AD-A081 117 OHIO STATE UNIV COLUMBUS ELECTROSCIENCE LAB F/G 17/9
ELECTROMAGNETIC SCATTERING FROM SIMPLE SHIP-SEA MODELS.(U)
DEC 77 J HUANG, W H PEAKE N00530-76-C-0186
UNCLASSIFIED ESL-(78)4428-3 NL

1 OF 1
AD A081 117

END
DATE FILMED
3-80
DDC

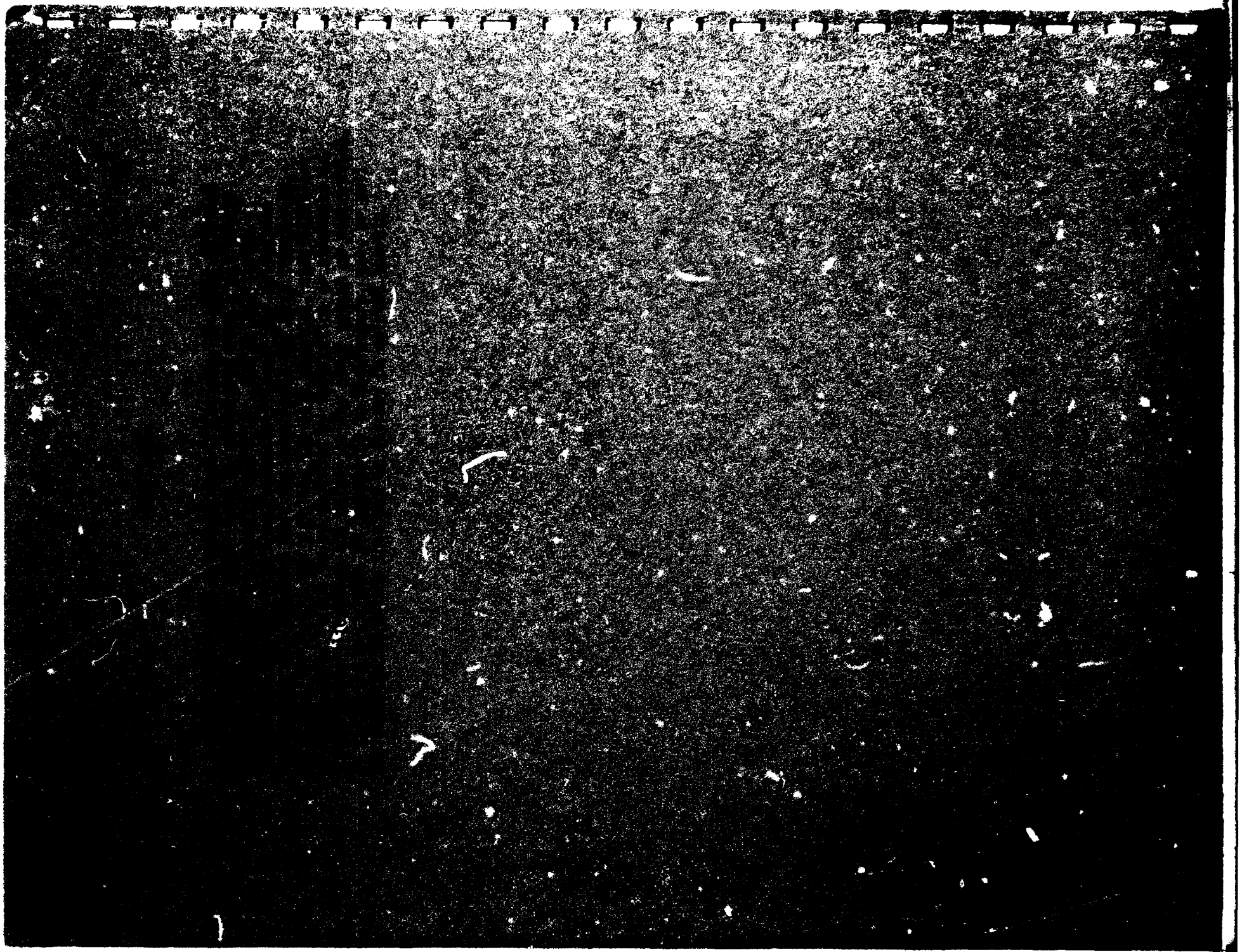

UNCLASSIFIED

SECURITY CLASSIFICATION OF THIS PAGE (When Data Entered)

REPORT DOCUMENTATION PAGE

READ INSTRUCTIONS BEFORE COMPLETING FORM

1 REPORT NUMBER: (9) Final rept. 19 May 76-19 Aug 77	2 GOVT ACCESSION NO. / 3 RECIPIENT'S CATALOG NUMBER
4 TITLE (and Subtitle): (6) ELECTROMAGNETIC SCATTERING FROM SIMPLE SHIP-SEA MODELS	5 TYPE OF REPORT & PERIOD COVERED: Final 5/19/76-8/19/77
	6 PERFORMING ORG. REPORT NUMBER: (14) ESL-(78)4428-3
7 AUTHOR(s): (10) Huang and W. H. Peake	8 CONTRACT OR GRANT NUMBER(s): (15) N60530-76-C-0186
9 PERFORMING ORGANIZATION NAME AND ADDRESS: The Ohio State University ElectroScience Laboratory, Department of Electrical Engineering Columbus, Ohio 43212	10 PROGRAM ELEMENT, PROJECT, TASK AREA & WORK UNIT NUMBERS: Project 3310-0421-76
11 CONTROLLING OFFICE NAME AND ADDRESS: Department of the Navy, Supply Office, Code 2524 Naval Weapons Center China Lake, California 83555	12 REPORT DATE: December 1977 / 13 NUMBER OF PAGES: 58
14 MONITORING AGENCY NAME & ADDRESS(if different from Controlling Office): (12) 58	15 SECURITY CLASS. (of this report): Unclassified / 15a DECLASSIFICATION DOWNGRADING SCHEDULE

16 DISTRIBUTION STATEMENT (of this Report)

DISTRIBUTION STATEMENT A
Approved for public release;
Distribution Unlimited

17 DISTRIBUTION STATEMENT (of the abstract entered in Block 20, if different from Report)

18 SUPPLEMENTARY NOTES

19 KEY WORDS (Continue on reverse side if necessary and identify by block number)

Radar cross-section
Ship signature
Composite surface
Ship-sea scattering model

20 ABSTRACT (Continue on reverse side if necessary and identify by block number)

Two models for calculating the interaction between a radar system and a ship at sea, both adapted to short range encounters, have been developed. The first utilizes a one dimensional composite surface to model the sea, and a flat plate to model the ship. Four major scattering mechanisms (Bragg scatter and specular scatter from the surface, reflection from the double bounce corner formed by plate and surface, and → next page

DD FORM 1 JAN 73 1473 EDITION OF 1 NOV 65 IS OBSOLETE

AD A 040251

UNCLASSIFIED

SECURITY CLASSIFICATION OF THIS PAGE (When Data Entered)

20.

edge diffraction by the plate) were identified, and the contribution of each to the total signature calculated by physical optics and GTD techniques. The signatures were in good agreement with measurements made at the Encounter Simulation Laboratory of the Naval Weapons Center. The second model was a two dimensional flat patch representation for the ocean, and an elliptic cylinder for the ship. GTD methods for calculating the signature due to the double bounce corner in this model have been completed. The signatures show a marked dependence on the direction of the radar trajectory with respect to the axes of the elliptic cylinder.

CONTENTS

I. INTRODUCTION

A problem of long standing in the design of radar systems has been that of detecting the presence and estimating the position of a ship at sea. Contemporary radar systems can exploit a variety of techniques, such as frequency agility, doppler filtering, time domain processing, polarization diversity, etc. to enhance the effective target contribution to the total return signal. However, the rational design of such systems must depend on a detailed understanding of the scattering characteristics of the target (i.e., the ship), the clutter background (i.e., the sea surface), and their interactions. Furthermore, the in-situ testing of such systems is expensive, and the results are often hard to interpret because one cannot reconstruct the precise encounter geometry (including the height distribution of the sea surface) at the moment of measurement.

Thus for a number of reasons, it is desirable to utilize mathematical modeling of the extended target complex represented by the ship in the presence of the sea surface. Such a model, once it has been properly validated, will also permit the economical design of a direct physical model of the encounter geometry. During the past two years, under Contracts N60530-75-C-0216 and N60530-76-C-0186, the ElectroScience Laboratory has;

(i) designed a one dimensional physical model of the ocean surface [1],

(ii) developed techniques for calculating the scattering from such a surface and relating it to the scattering from the ocean [1,2,3],

(iii) developed simplified ship-sea models in which the interaction term (the major contribution to the total signal) can be identified and calculated.

It is the purpose of this report to describe these simplified ship sea models, including the sea-surface models, in detail; to review the techniques for calculating the several terms in the total radar signature from such models; and to compare a number of calculated signatures with measurements carried out at the Encounter Simulation Laboratory of the Naval Weapons Center.

II. REVIEW OF PREVIOUS WORK, AND GENERAL APPROACH TO SHIP-SEA MODELS

A number of significant steps have already been taken towards the development of a complete near-field ship-sea model. The first phase was to design a physical surface which had the same scattering mechanisms as the sea surface, in order to provide both an inexpensive physical

model of the sea surface, and to validate mathematical models for determining the scattered fields. The bistatic scattering behavior of the sea surface alone is quite complex, but is now understood fairly well in terms of the "composite" model. In this model, the scattering near the specular direction (i.e., near normal incidence for back scatter) is controlled by the slope distribution of the large scale structure of the surface. This part of the scattering is then calculated by the physical optics model, and provides an explanation not only for the near normal back scatter but also for the dependence of brightness temperature on polarization and wind speed (at least at the lower wind speeds). For off-normal incidence the back-scattering mechanism is the "Bragg-scatter" from capillary and short wavelength components of the ocean surface. This part of the scattering is calculated by perturbation theory and when combined with the known height spectrum of the ocean it explains the angular and polarization dependence of the radar cross-section, and the weak dependence on electromagnetic wavelength and wind speed. Thus the problem in specifying a suitable physical surface model is to select one which will have a height spectrum which satisfies the Bragg condition for the given experimental geometry (for back scatter away from normal incidence), has an effective mean square slope equivalent to the desired ocean surface (for forward scatter or back scatter near normal incidence) and, would be compatible with the geometrical and other constraints imposed by the practical limitations of the Encounter Simulation Laboratory of the Naval Weapons Center.

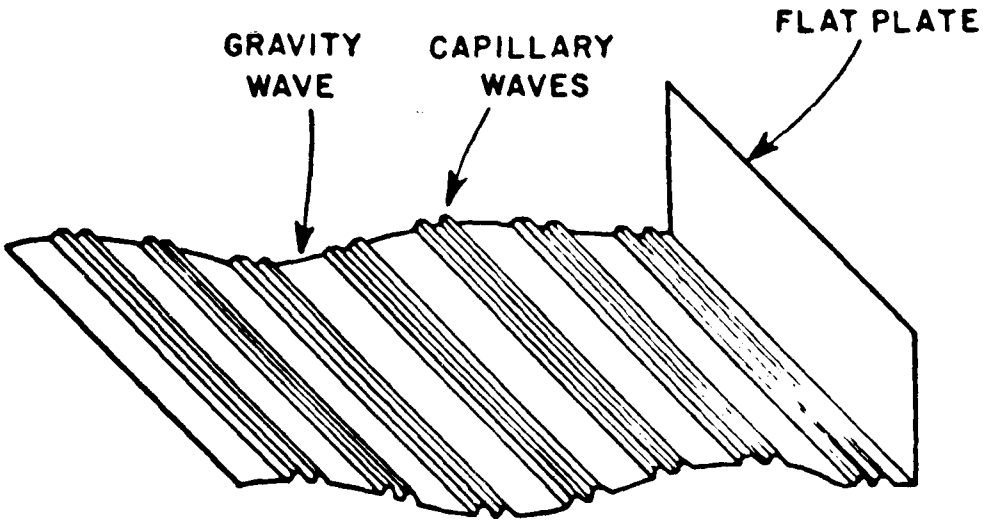

Figure 2-1. Composite sea surface-ship model.

The final design of the surface is reported in Reference [1], and is illustrated in Figure 2-1. The relation between the structural form of the surface and the scattering mechanisms of the ocean are discussed in more detail in Reference [1]. In general, however, the large undulations represent the large scale (gravity wave) structure of the ocean and the small corrugations provide Bragg scatter from the small scale structure. Three mathematical models (physical optics, perturbation theory, moment method) were developed to calculate the scattering from this composite surface, and these are described in detail in References [1-3]. It was found, as expected, that the physical optics model provided an accurate prediction of the scattered field near the specular direction. Away from the specular direction, it was expected that the scattered fields would be calculated by perturbation theory, but it was found that while the general level, and the polarization dependence were correct, the detailed field structure was not well predicted. In order to achieve better agreement with measured data, the modified moment model [2] was developed. In this model, the moment method is used to estimate the exact surface currents over a single period or cell of the small scale structure, and the total signature computed from the sum of these individual cell currents. This modified moment method produced signatures in excellent agreement with the measured back-scattering signatures. Furthermore, a comparison of the measured and calculated radar cross-section of the composite surface with the known cross-section of the ocean showed that both of the known ocean scatter mechanisms were appropriately modelled. Thus the next step in developing a complete model for the interaction of radar system with a ship at sea is to produce a model for the ship which will be complex enough to exhibit all the major scattering mechanisms of the actual situation, but still simple enough so that the scattered fields may be readily computed.

In undertaking the development of these simplified ship-sea models, two separate approaches have been taken. The first approach considered a model which could easily be implemented using the composite surface already constructed at the Encounter Simulation Laboratory (Figure 2-1). This would permit actual measurements (subsequently carried out by Naval Weapons Center) of typical signatures, which could be compared with calculated signatures and thus validate the theoretical basis of the model. This model, the techniques for calculating the signatures, and a comparison with the measured signatures, are described in more detail in Section IV.

The second approach was the development of a model more representative of an actual encounter geometry, utilizing a two dimensional sea surface (discussed in section III), and a simple, but three dimensional ship model. This ship-sea model is discussed in section V.

III. MODELS FOR THE SEA SURFACE

Before undertaking the construction of the ship-sea models in their entirety, it will be useful to develop an appropriate model for the sea surface. Three different sea surface models have been considered, and are described briefly below.

(i) Distribution of Specular Points

It is known [4] that the specular component of scatter from the sea surface at microwave frequencies can be calculated by assuming that the scattering is essentially a reflection process from a number of bright spots, (stationary phase points) characterized by their position and height ζ_i above the mean surface, and their gaussian curvature g_i. In this case, the scattering cross-section σ_B of a portion of surface containing N bright spots is given by

$$\sigma_B = \left| \sum_1^N \pi^{1/2} \, g_i^{1/2} \, e^{-jk(r_i+r_i')} \, R(\nu) \right|^2 \qquad (3\text{-}1)$$

where r_i, r_i' are the distances from the bright spot to transmitter and receiver respectively (see Figure 3-1), k is the electromagnetic wave number, ν is the local angle of incidence, and R is a polarization dependent reflection coefficient. Both the probability distribution for the curvatures, and for the distribution of bright spot heights, are known for the sea surface, since they can be found from the joint height distribution function for the surface [4]. Thus it is possible, using these distributions, to produce a model surface which is composed of a number of randomly distributed spherical or ellipsoidal sections whose height and curvatures are appropriately chosen (see Figure 3-1). This model should provide a good estimate of the scattered field strength at any point. Unfortunately, the problem of tracking the positions of these stationary phase points as both transmitter and field point move is a formidable one. In addition, the number N_a of points per unit area of surface is approximately (for back scatter, for example)

$$N_a = 7{\cdot}2 \, s^2/(4\pi h^2) e^{-\tan^2\nu/s^2} \qquad (3\text{-}2)$$

for a plane wave incident at an angle ν, for a surface with rms height h^2, and rms slope s^2. A sea surface area of even a few thousand square meters would possess an extremely large number of such specular points. For these reasons (and because the specular point model does not account for the Bragg scatter component) the specular point model was rejected for the purposes of this report.

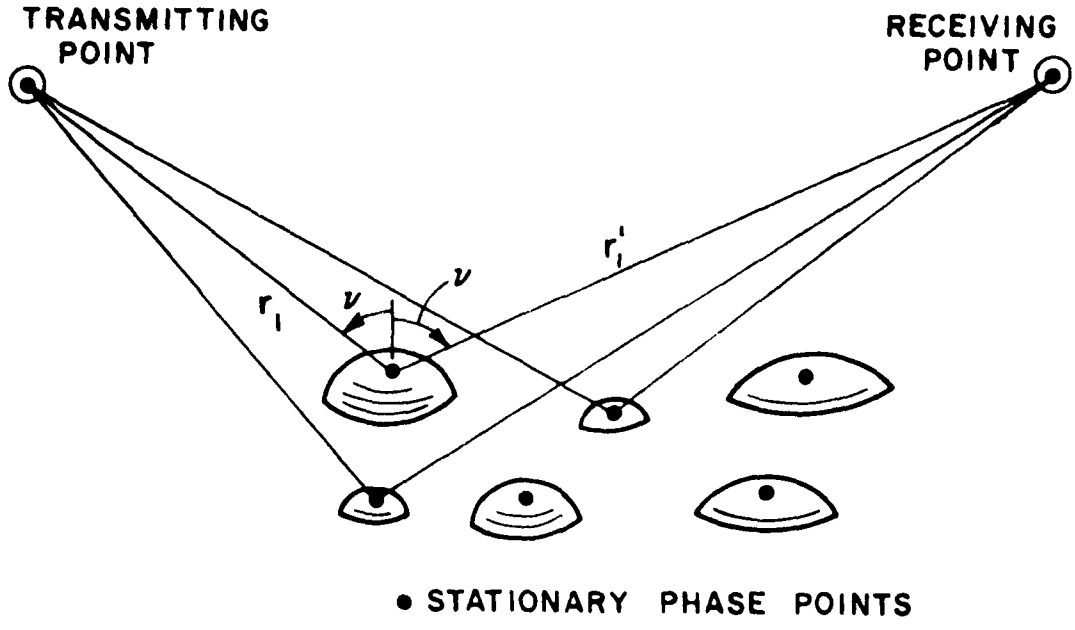

Figure 3-1. The specular point model for the sea surface.

(ii) The Explicit Surface Representation

The second surface model to be considered was one which uses an explicit representation of the surface height z as a Fourier series. For a square area of side L, the sea surface height has the expansion

$$z(xyt) = \sum_{m,n} A_{mn} \cos \frac{2\pi}{L} (mx + ny + w_{mn} t + \phi_{mn})$$

where

$$k_{mn}^2 = (2\pi/L) (m^2+n^2)^{1/2}$$

is the mechanical wave number and w_{mn} is the angular frequency of a component traveling wave of phase ϕ_{mn}. Here k_{mn} and w_{mn} are connected by an appropriate dispersion relation, for example $w_{mn}^2 = g\, k_{mn}$ for gravity waves. However, even if the amplitudes A_{mn} were chosen to be

compatible with the known height spectrum of the ocean (e.g., $A_{mn} = B/k_{mn}^2$ for a Phillips spectrum) this representation cannot easily be made realistic. This is because the coefficients and phase angles must be chosen in such a way as to reproduce not only the cruder statistical properties of the surface (spectrum, height distribution) but also those unique features of the real sea (cuspedness, upwind skewed slope distribution, etc.) which are significant for the scattering problem. Thus, for example, the problem of cuspedness might be approached by expanding the smaller wave number components in one of the canonical wave profiles (i.e., trochoids) rather than sinusoids. However, even if a suitable surface representation could be found, as a scattering model it suffers from the same disadvantages as the specular point model. This is that the direct calculation of the scattering from such a surface (e.g., by integrating "physical optics" currents over the surface) would require impractically long computation times.

(iii) The Flat Patch Model

To avoid the computational difficulties of these surface models, it was decided to adopt a simpler approach to the surface scattering problem. The model chosen is the "flat patch" model in which the actual sea surface is replaced by a flat surface divided into squares or rectangles (see Figure 5-2). The scattering, including time delay and doppler shift, is referred to a conveniently chosen point (usually the center) of the rectangle. The magnitude of the scattered field in any direction is then determined by the size of the rectangle and the square root of the bistatic radar cross-section per unit area. The ensemble average signature produced by such a model should agree fairly well with the average signatures produced by the specular point or surface representation models. This is because the radar cross-section is itself derived from a specular point model. However, to obtain an individual signature more representative of an actual signature, it may be desirable to associate a random phase shift with the return from each patch.

The only remaining parameter in the model is the choice of patch size. In practice, the area of the patches are probably most conveniently chosen empirically, by reducing their size and increasing their number until the statistical properties of the return show no significant change. A more detailed description of the patch model is given in section V.

IV. THE "ONE-DIMENSIONAL" SHIP-SEA MODEL

(i) Introduction

The first simplified ship sea model to be considered was an extension of the Naval Weapons Center Composite Surface (see Figure 2-1), as described in Reference [1]. The ship is represented by a flat plate at the end of the surface. Even this simple model provides examples of

the four principal scattering mechanisms which would contribute to a radar signature in a real encounter. These are (i) Bragg type back-scattering from the trapezoidal structure, which represents the "clutter" signal in the absence of the ship target; (ii) specular back scatter from the sinusoidal structure, which contributes to the clutter level at scattering angles near normal incidence; (iii) forward scatter from transmitter to surface to flat plate to receiver, which represents the double bounce corner mechanism (the predominant interaction between sea surface and target); (iv) the field diffracted by the edge of the metal plate, which represents direct diffraction by the target alone.

In this section two separate approaches to calculating the signatures of this one dimensional ship sea model are described. In the first, a physical optics technique similar to that of References 1-3 is used. In the second approach, the methods of geometrical optics and the geometrical theory of diffraction (GTD) are used to calculate all mechanisms except the Bragg scatter from the trapezoidal structure. The reason for this dual approach is that the first method (physical optics) has been shown in Reference 1 to provide an effective, though not particularly rapid, method for calculating the scattering from the composite surface. However, in calculating the signatures for more realistic ship-sea models, it is expected that GTD techniques will be used, since the programs are faster, and since GTD is known to be effective in computing the scattering from aircraft and similar complex objects. Thus to validate the GTD approach for these future studies, it was considered desirable to compare the GTD results with physical optics results known to be in good agreement with experiments.

(ii) The Physical Optics Technique

The physical optics approximation finds the fields scattered due to an incident magnetic field H_i by using the approximate surface current distribution $J_s = 2\hat{n} \times H_i$. A detailed discussion of the physical optics fields scattered by the composite surface alone is given in Reference [1]. The application of physical optics to the ship-sea model of Figure 2-1 together with a number of comparisons with experimental signatures, is given in detail in Reference [5]. In this report we summarize briefly the principal results of Reference [5].

Referring to Figure 4-1, if the surface with generators in the x direction has the profile $z = h(y)$, the radar trajectory has dive angle ψ, antenna depression angle α, and the range to the mean surface along the boresight is R_o, then the receiver voltage (Reference [5]) is

$$V_r = \frac{2jV_o}{4\pi} \int_y \bar{X} \frac{(R_o\cos(\theta-\psi) + y\sin\psi - h\cos\psi)}{\cos\psi[(h-R_o\cos\theta)^2 + (y+R_o\sin\theta)^2]^{1/2}} * e^{\frac{B}{2}(y\cos\theta+h\sin\theta)^2/R_2^2} e^{-\frac{B}{2}(h\cos\theta-y\sin\theta)^2/R_2'^2} dy \qquad (4\text{-}1)$$

where

ϕ = surface normal angle

$R_2 = R_o + y \sin\theta - h \cos\theta$

$R_2' = R_o' - y \cos\beta - h \sin\beta$

V_o = reference voltage level

$\beta = \theta + \pi/2$ angle between y axis and boresight.

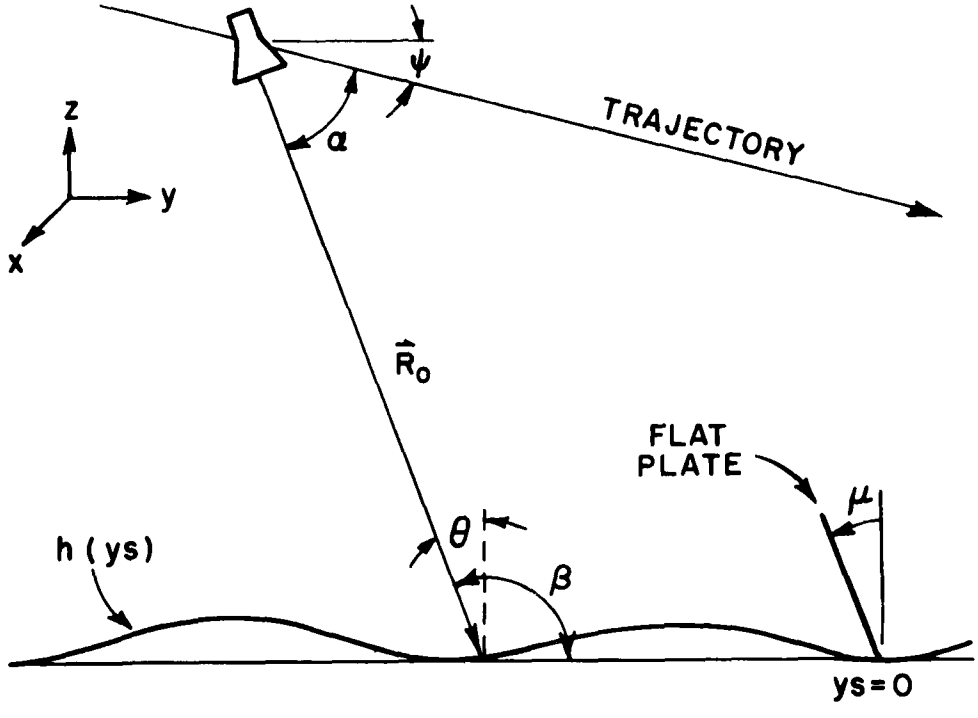

Figure 4-1. Geometry of input variables.

The term $\underline{X}$, the result of integrating over the surface generators, is given by

$$\underline{X} = \frac{-R_2 R_2' \sqrt{2\pi}\, e^{-jk(R_1+R_1')}}{[AR_1^2 R_1'^2 R_2'^2 + AR_1^2 R_1'^2 R_2^2 + jkR_1 R_1'^2 R_2^2 R_2'^2 + jkR_1' R_1^2 R_2^2 R_2'^2 + R_1'^2 R_2^2 R_2'^2 + 3R_1^2 R_2^2 R_2'^2]^{1/2}} \tag{4-2}$$

with

$$R_1^2 = (h-R_o\cos\alpha)^2 + (y+R_o\sin\alpha)^2$$

$$R_1'^2 = (h-R_o'\sin\beta)^2 + (y-R_o'\cos\beta)^2$$

and it has been assumed that the antenna pattern is gaussian in both planes with pattern $\exp(-A\tan^2\eta)$ in the plane defined by the bore sight and the x axis, and pattern $\exp(-B\tan^2\xi)$ in the plane defined by the boresight and the trajectory. By evaluating the integral over the surface profile, the contribution of the sinusoidal (gravity wave) structure and the composite surface (sinusoidal plus trapezoidal structure) can be found. The target contribution due to the double bounce corner may also be evaluated, using the same integral, by exploiting a number of simplifications introduced by image theory. The fourth contribution to the total signature, that due to edge diffraction must be calculated by GTD (see section IV-iii). A detailed derivation of the form of these four components, and a computer code for determining the resulting signatures, is given in Reference [5].

As an example of the use of Equation (4-1), Figures 4-2 and 4-3 show the four components of the total signature for two encounter geometries. In these figures, the distance scales YY represent the y co-ordinate of the radar with respect to the position of the corner plate, and the ordinate represents receiver voltage (in dB) with respect to a nominal reference level. In each figure the first signature is the contribution of the gravity waves alone, and the second signature is the backscatter from the composite surface (sinusoid plus trapezoid surface). Note that the large lobe towards YY = 0 is an artifact of the program caused by terminating the integration at the end of the surface. The third and fourth signatures in Figures 4-2 and 4-3 show the double bounce corner and the edge diffraction terms respectively. The fifth signatures show the predicted total signature (the sum of the four components) compared with signatures measured at the Naval Weapons Center. In both figures the absolute level of the measured signature was adjusted so that the measured and calculated levels for a calibration sphere were brought into correspondence. Both signatures include the effects of range gate and receiver processing (detector and low pass filter). From these figures, and the numerous signature comparisons given in Reference [5], it is clear that the physical optics technique can give good agreement with experimental results for the simplified one dimensional ship-sea model.

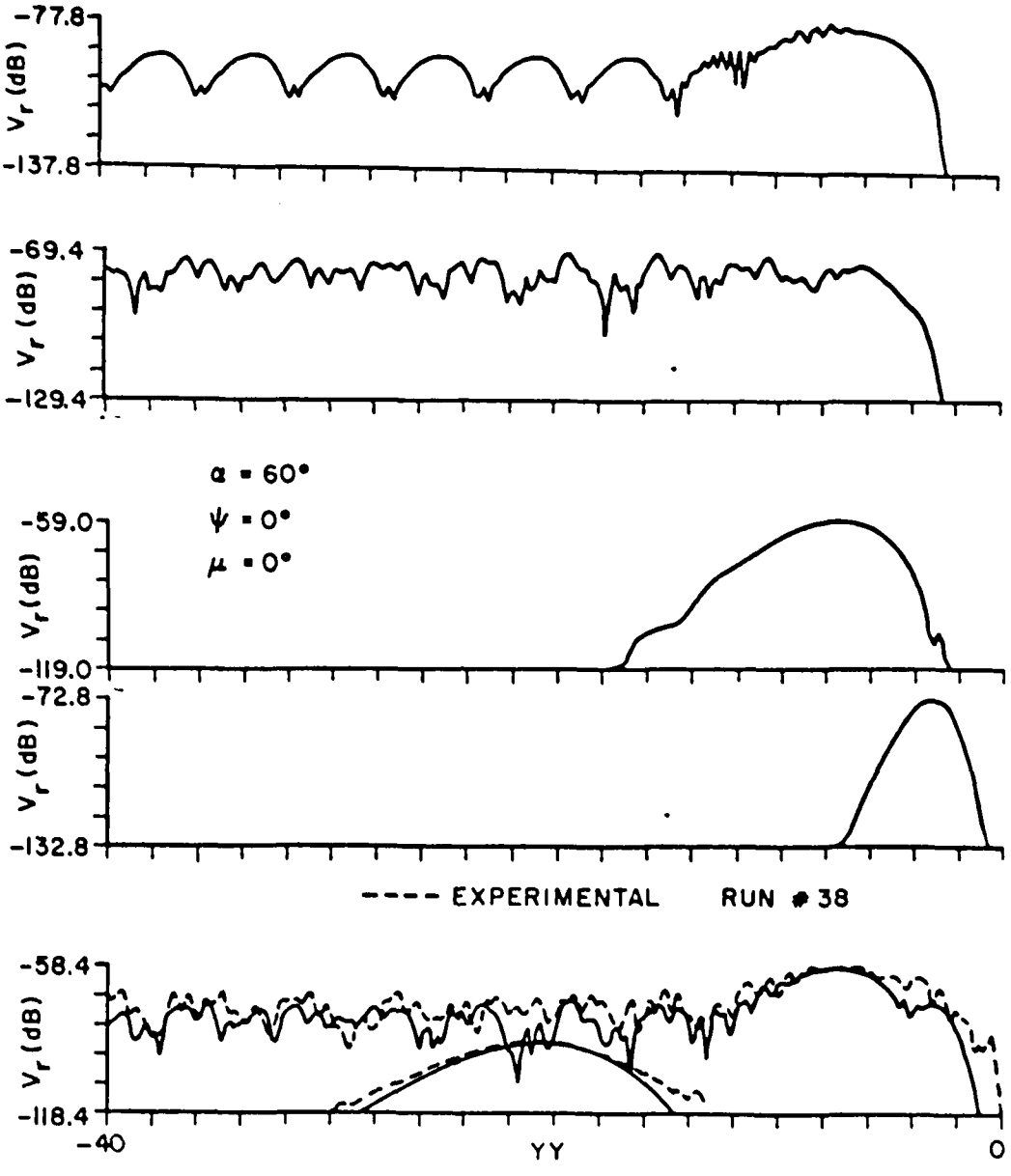

Figure 4-2. Component parts of the voltage signature for the simplified ship sea model. From top to bottom the signatures show the gravity wave signature, the composite surface signature, the double bounce corner, the edge diffraction contribution and the total (composite signature). The bottom signature is compared with an experimental run for the same geometry. (Note sphere return at YY ≃ -20) Antenna depression angle α=60°. Dive angle ψ=0°. Plate angle μ=0°.

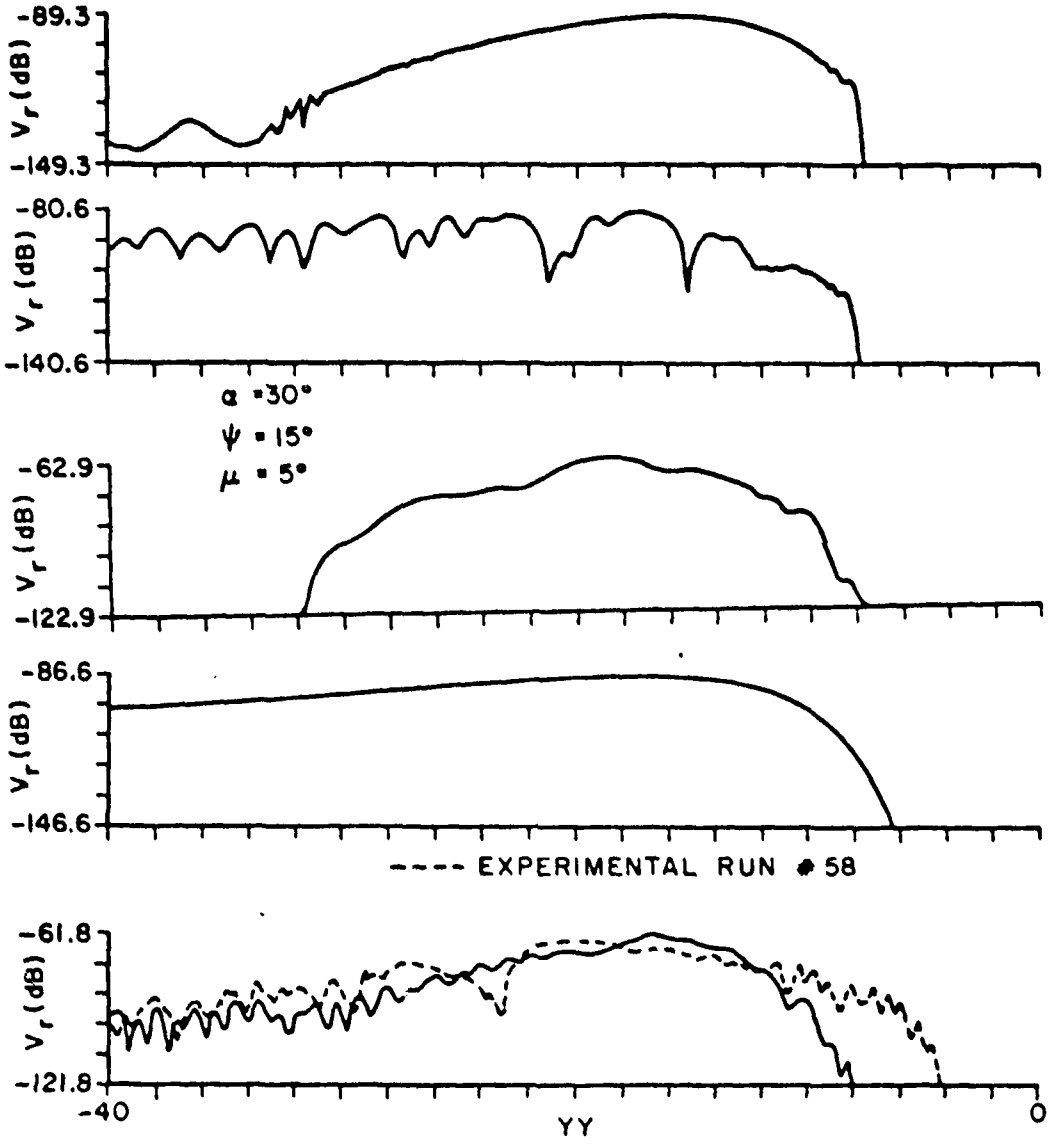

Figure 4-3. Component parts of the voltage signature for the simplified ship sea model. From top to bottom the signatures show the gravity wave signature, the composite surface signature, the double bounce corner, the edge diffraction contribution and the total (composite signature). The bottom signature is compared with an experimental run for the same geometry. (Note sphere return at YY ≈ -20) Antenna depression angle α=30°. Dive angle ψ=15°. Plate angle μ=5°.

(iii) Introduction to the GTD Model

In order to validate the computationally efficient methods of geometrical optics and GTD for application to more complex ship-sea models, it was decided to apply them first to the same one-dimensional surface and target (Figure 2-1) discussed in the previous section.

The specific geometry analyzed is shown in Figure 4-4. The sea surface is represented by the one dimensional sinusoidal profile, and the simplified ship model is the eight-foot flat plate located at the end of the sea surface. The antenna behaves as both a transmitter and a receiver as it moves along the indicated antenna path. To reduce the complexity of the computations, only the case of the μ=90° corner is considered. However, it is not difficult to modify the procedure to handle any angle μ.

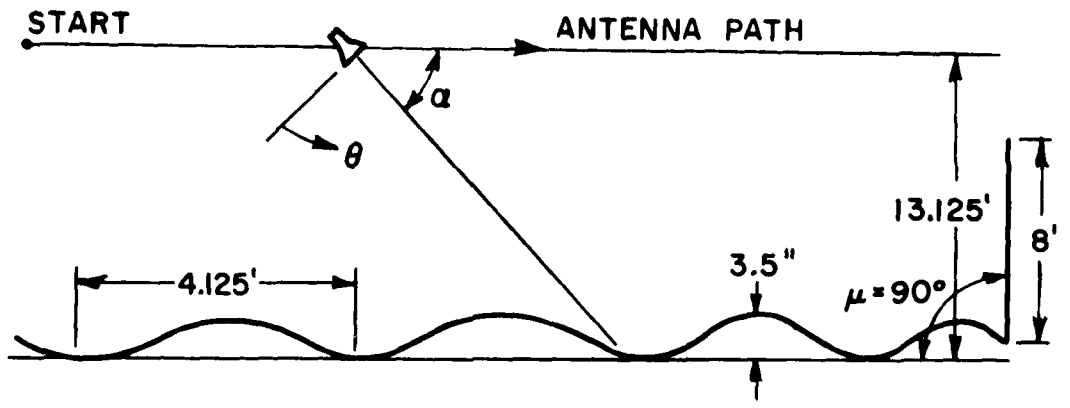

Figure 4-4. 2-dimensional geometry of the simplified ship-sea model.

The major scattering mechanism to be calculated by the GTD method is the double-reflected field between the sinusoidal surface and the vertical plate. A numerical search technique, via the law of reflection, is used to find all the specular points on the sinusoidal surface; then all the rays from these specular points to the flat plate and back to the receiver are summed to obtain the scattered field at the receiver. In addition, the diffracted field from the edge of the plate is also calculated.

Since the vertical plate and the sinusoidal surface are cylindrical structures, and both the antenna boresight and the antenna path are in the principal plane of the geometry shown in Figure 4-4, a two dimensional analysis is adequate. In addition, since the antenna is in the near field of the sinusoidal surface and the vertical plate, a near field analysis is required. In the sections that follow, a procedure is first described to find the specular points. These points are then used to calculate the double bounce (reflected) fields, and the edge diffracted component.

(iv) Patterns and Incident Fields of the GTD Model

1. Antenna pattern and the field incident on the sinusoidal surface

The antenna pattern is assumed to have a 15-degree half-power beamwidth with a gaussian distributed pattern function. Since the field points are in the near field of the antenna, it might appear that a composite source (i.e., an array of elements) would be required; however it was found from the results that a single infinitesimally small element with a gaussian pattern function was sufficient. This simplification saves a tremendous amount of computer time.

The gaussian pattern function is given by

$$f(\theta) = \exp[-(ka\cos\theta)^2/4\pi] \qquad (4\text{-}3)$$

where

$k = 2\pi/\lambda$

a = constant that determines the beamwidth

θ = pattern angle defined in Figure 4-4.

For a "horizontally" polarized antenna, the radiated field is given by

$$\vec{E}^i(\theta,s) = C_1 \cdot f(\theta) \cdot \frac{e^{-jks}}{s} \hat{\phi} \qquad (4\text{-}4)$$

For a "vertically" polarized antenna (the E-field vector is parallel to the plane of incidence), the radiated field is given by

$$E^{i}(\theta,s) = C_2 \sin\theta \; f(\theta) \cdot \frac{e^{-jks}}{s} \qquad (4\text{-}5)$$

where C_1 and C_2 are appropriate constants, and s is distance from the source to the field point.

2. Law of reflection and the numerical search technique

In order to find the field reflected off the sinusoidal surface in a given direction d as shown in Figure 4-5, the reflection point must first be found. The point of reflection must satisfy the law of reflection which states that the angle of incidence is equal to the angle of reflection that is

$$-\hat{i} \cdot \hat{n} = \hat{d} \cdot \hat{n} \qquad (4\text{-}6)$$

and that the incident, reflected and surface normal vectors must lie in the same plane,

$$\hat{i} \times \hat{n} = \hat{d} \times \hat{n} \qquad (4\text{-}7)$$

$\hat{i}$ = unit vector from source to reflection point

$\hat{n}$ = unit surface normal

$\hat{d}$ = unit vector from reflection point to image point.

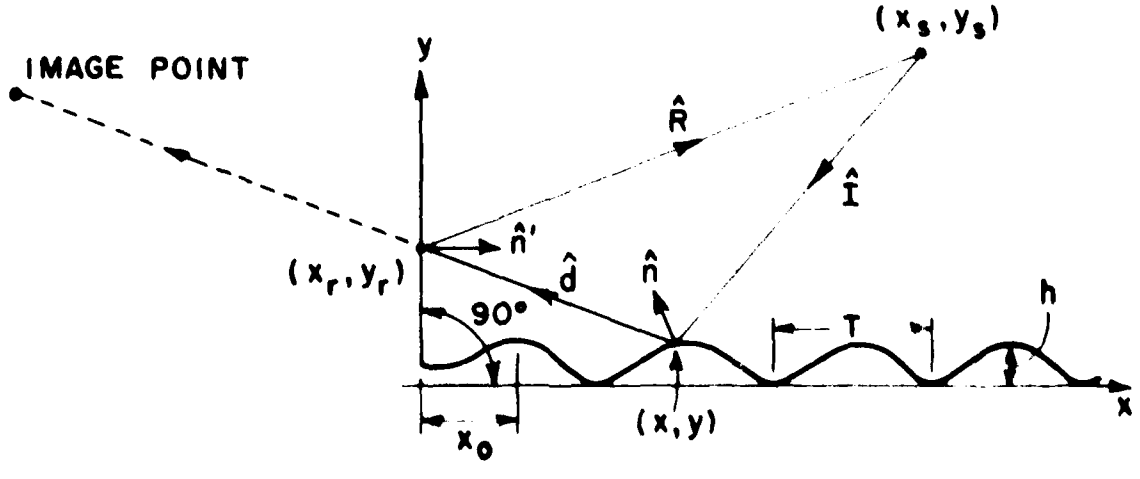

Figure 4-5. Double-reflection configuration.

These equations can be combined as

$$(\vec{n} \times \vec{I})(\vec{n} \cdot \vec{d}) + (\vec{n} \cdot \vec{I})(\vec{n} \times \vec{d}) = 0 \qquad (4\text{-}8)$$

To find the reflection point, the following expressions are needed (see Figure 4-4):

$$\text{curved surface equation: } y(x) = h \cos\left[\frac{2\pi}{T}(x-x_o)\right] \qquad (4\text{-}9)$$

$$\text{slope of surface: } \frac{dy}{dx} = -\frac{2\pi h}{T} \sin\left[\frac{2\pi}{T}(x-x_o)\right]$$

$$\text{tangent to the curve: } \vec{t} = \hat{x} + \frac{dy}{dx}\hat{y}$$

$$\text{normal to the curve: } \vec{n} = -\frac{dy}{dx}\hat{x} + \hat{y} \qquad (4\text{-}10a)$$

$$\text{unit normal: } \hat{n} = \frac{-dy/dx\,\hat{x} + \hat{y}}{\sqrt{1 + (dy/dx)^2}} \qquad (4\text{-}10b)$$

$$\text{incident vector: } \vec{I} = (x-x_s)\hat{x} + (y-y_s)\hat{y} \qquad (4\text{-}11a)$$

$$\text{reflection vector: } \vec{d} = (x_r-x)\hat{x} + (y_r-y)\hat{y} \qquad (4\text{-}11b)$$

Substituting equations (4-10) and (4-11) into (4-8), one finds

$$f \quad (n_x I_x + n_y I_y)(n_x d_x - n_y d_x) + (n_x d_x + n_y d_y)(n_x I_y - n_y I_x)$$

$$= \left[(x_s-x)\frac{dy}{dx} + (y-y_s)\right]\left[(x-x_r) - \frac{dy}{dx}(y_r-y)\right] +$$

$$+ \left[(x-x_r)\frac{dy}{dx} + (y_r-y)\right]\left[(x_s-x) + \frac{dy}{dx}(y_s-y)\right] = 0 \qquad (4\text{-}12)$$

One needs to find all the reflection points on the sinusoidal surface under the condition that the point (x_r, y_r) be so located that the vector R is directed toward the point (x_s, y_s). Since the wall is a flat metal surface, the vector d is directed straight toward the image source point behind the wall as shown in Figure 4-5. Hence in Equation (4-12) one should replace the point (x_r, y_r) by $(-x_s, y_s)$.

Since Equation (4-12) is very complicated and very time consuming if it is to be solved repeatedly, a numerical search technique (incremental method) is utilized to find all the specular points. The method is based on the first term in a Taylor series expansion of the reflection-point equations (Equation (4-12)) such that the equations for the new reflection point (f_{j+1}) is given in terms of the equation of the last point (f_j) by

$$f_{j+1} = f_j + df_j$$

where

$$df_j = \frac{\partial f_j}{\partial x_s} \delta x_s + \frac{\partial f_j}{\partial y_s} \delta y_s + \frac{\partial f_j}{\partial x} \delta x$$

Because f_{j+1} must also satisfy the reflection equation, it implies that $f_{j+1} = 0$ or $f_j + df_j = 0$ so that

$$\delta x = \frac{-\left[f_j + \frac{\partial f_j}{\partial x_s} \delta x_s + \frac{\partial f_j}{\partial y_s} \delta y_s\right]}{\frac{\partial f_j}{\partial x}} \qquad (4\text{-}13)$$

The above equation says that as the source moves by an incremental distance $(\delta x_s, \delta y_s)$ the reflection point in the sinusoidal surface will move by an incremental distance δx. In this way if all the reflection points are once found, they can be tracked by Equation (4-13) while the source changes position in small increments.

*In the event that $\alpha \neq 90°$, x_r and y_r would re replaced by the coordinates of the image of the source as imaged by the reflecting flat plate.

(v) The Reflected Field

After the specular points have been found, the doubly reflected field for each specular point is computed using the geometry illustrated in Figure 4-6.

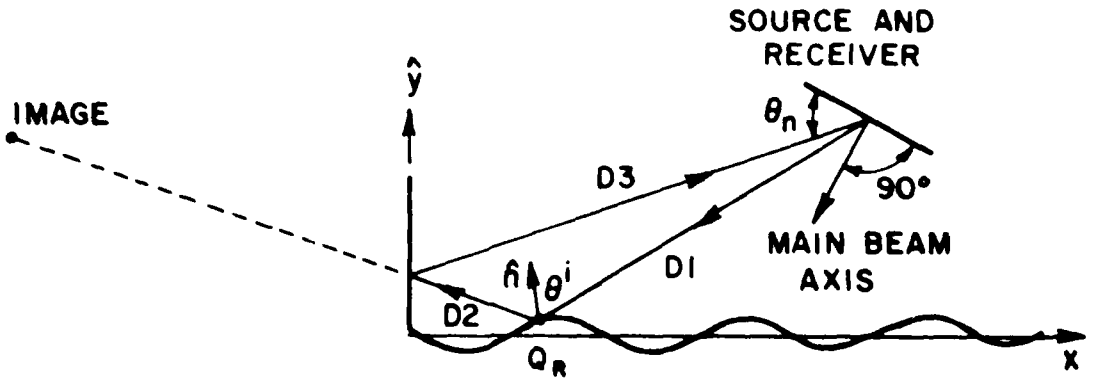

Figure 4-6. Double-reflection configuration.

The reflected field from a curved surface is given in terms of geometrical optics for the 3-D case by [6]

$$\bar{E}^r(s) = \bar{E}^i(Q_R) \cdot \bar{\bar{R}} \sqrt{\frac{\rho_1^r \rho_2^r}{(\rho_1^r+s)(\rho_s^r+s)}}\; e^{-jks} \qquad (4\text{-}14)$$

where s is the distance traveled by the reflected ray. In this case s = D2 + D3 (see Figure 4-6) $E^i(Q_R)$ is the incident electric field at the point of reflection Q_R and ρ_1^r, ρ_2^r are the principal radii of curvature of the reflected wavefront;

$$\frac{1}{\rho_{1,2}^r} = \frac{1}{s'} + \frac{1}{\cos\theta^i}\left[\frac{\sin^2\theta_2}{R_1} + \frac{\sin^2\theta_1}{R_2}\right] \pm \sqrt{\frac{1}{\cos^2\theta^i}\left[\frac{\sin^2\theta_2}{R_1} + \frac{\sin^2\theta_1}{R_2}\right]^2 - \frac{4}{R_1 R_2}}$$

where s' = D1 is the distance between source and the reflected point

θ^i is the angle of incidence with $\cos\theta^i = -\hat{n} \cdot \hat{I} = \hat{n} \cdot \hat{d}$

θ_1 is the angle between the incident ray and the vector tangent to the surface in the x-y plane at the reflection point

θ_2 is the angle between the incident ray and the vector tangent to the surface in the z-plane

R_1 and R_2 are radii of curvature of the curved surface.

For the two dimensional case, $R_2 = \infty$ and $\theta_2 = 90°$. Thus one finds that

$$\rho_1^r = \frac{s' R_1 \cos\theta^i}{2s'+R_1\cos\theta^i} \quad \text{and} \quad \rho_2^r = s'$$

$$R_1 = \frac{[1+y'(x)]^{1.5}}{|y''(x)|} \text{sign}[y(x)] \tag{4-15}$$

$\bar{\bar{R}}$ is the dyadic reflection coefficient such that

$$\bar{\bar{R}} = \begin{cases} 1 & \text{for vertically polarized incident wave (electric vector parallel to the plane of incidence)} \\ -1 & \text{for horizontally polarized incident wave (electric vector perpendicular to the plane of incidence)} \end{cases}$$

It is necessary to sum the fields calculated by Equation (4-14) from all the specular points for any instantaneous source location to form the total double-bounce reflected field. All fields that are reflected back to the receiver are multiplied by the appropriate antenna pattern function, giving

$$\bar{E}^r_{\text{received}} = \sum_{n=1}^{N} \bar{E}^i_n(Q_R) \sqrt{\frac{\rho_1^r \cdot D1}{(\rho_1^r+D2+D3)(D1+D2+D3)}}\, e^{-jk(D2+D3)} \cdot f(\theta_n) \tag{4-16}$$

The field traveling in the reverse direction will yield the same amount of energy as that shown in Figure 4-6, by the theorem of reciprocity, so that the total received field due to double reflection is twice that calculated by the above equation.

(vi) Diffracted Fields

Any ray that reaches the upper tip of the vertical wall will excite a set of edge diffracted rays that radiate into all directions. In the present analysis there are two major types of diffracted rays. The first type, termed a reflected-diffracted ray, is associated with a ray reflected by the sinusoidal surface and diffracted by the tip of the plate. The second type, called a diffracted ray, is associated with a ray that comes directly from the antenna and is subsequently diffracted. The GTD is applied here to analyze these two terms. In order to define a number of parameters and functions used in the GTD, it is essential to discuss first the three-dimensional wedge diffraction problem (see Figure 4-7).

The source, which radiates the field $\vec{E}^i(s)$, is located at point $\bar{s}'$. It can be an arbitrary electric or magnetic source causing plane, cylindrical, or spherical wave incidence on the edge. The diffracted vector field $E^d(\bar{s})$ at the observation point $\bar{s}$ can be written in terms of a dyadic diffraction coefficient [7],

$$\vec{E}^d(\bar{s}) = \vec{E}^i(Q_E) \cdot \bar{\bar{D}}\, A(s) e^{-jks} \qquad (4\text{-}17)$$

where

$$\bar{\bar{D}} = -\hat{\beta}_o'\hat{\beta}_o\, D_s - \hat{\phi}'\hat{\phi}\, D_h$$

and s is distance between diffraction point and receiver. The quantity A(s) is a ray divergence factor given by

$$A(s) = \sqrt{\frac{s'}{s(s+s')}}$$

for spherical wave incidence where s' is distance between source and diffraction point. The edge diffracts a cone of rays such that $\beta_o = \beta_o'$ (see Figure 4-7) so that the ray-fixed coordinate system is centered at the point of diffraction Q_E. The relationship between the orthogonal unit vectors associated with these coordinates ($\beta_o, \phi, \hat{D}$; $\beta_1', \phi', \hat{I}$) are given by

$$\hat{I} = \hat{\beta}_o' \times \hat{\phi}' \qquad \hat{D} = \hat{\beta}_o \times \hat{\phi}.$$

The diffraction coefficients for soft and hard boundary conditions are given by

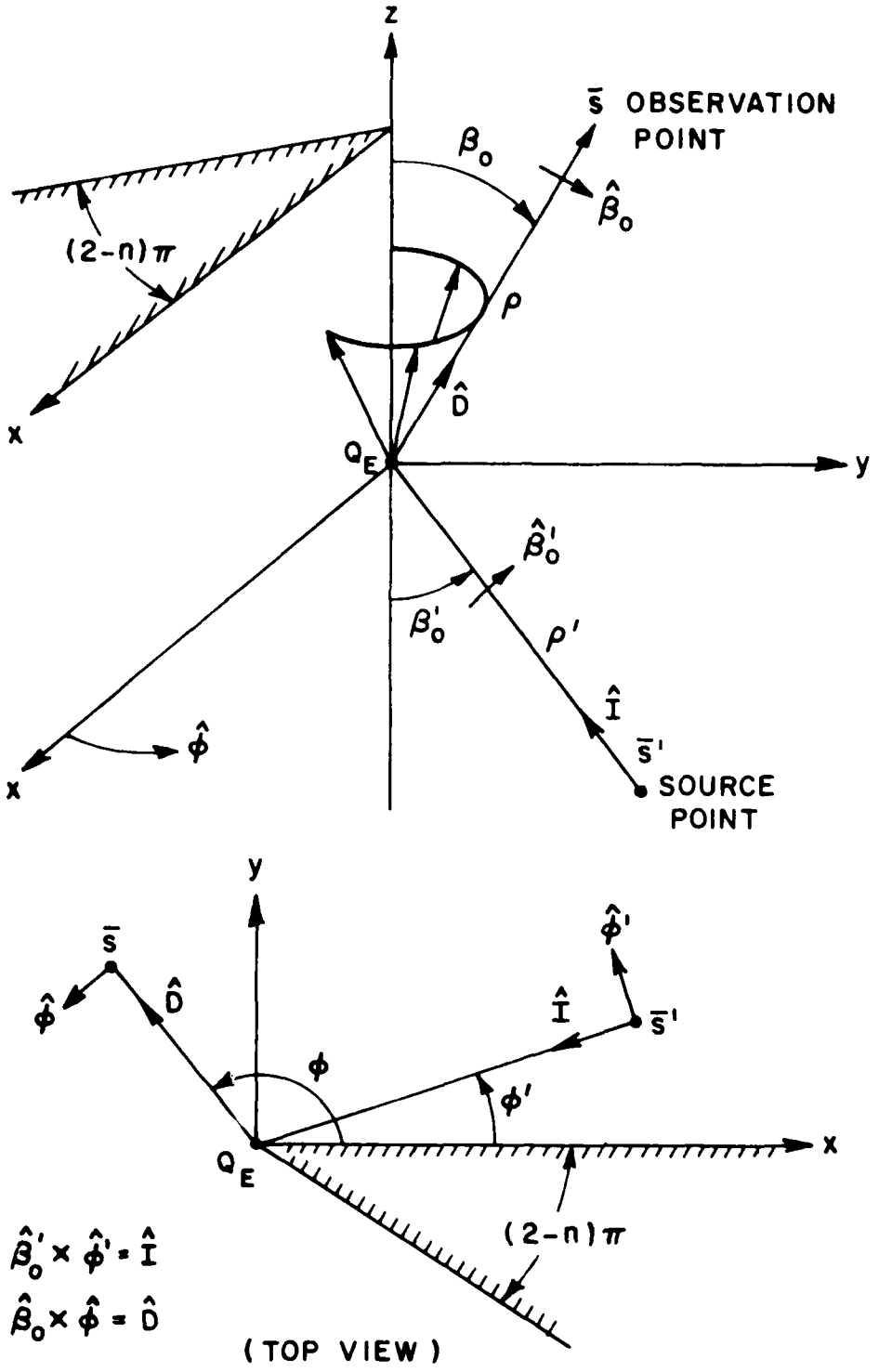

Figure 4-7. Geometry for three-dimensional wedge diffraction.

$$D_{s,h}(\phi,\phi';\beta_o) = \frac{-\exp(-j\pi/4)}{2n\sqrt{2\pi k}\,\sin\beta_o}\left\{\cot\left(\frac{\pi+(\phi-\phi')}{2n}\right)F[kLa^+(\phi-\phi')]\right.$$

$$+ \cot\left(\frac{\pi-(\phi-\phi')}{2n}\right)F[kLa^-(\phi-\phi')] \mp \cot\left(\frac{\pi+(\phi+\phi')}{2n}\right)F[kLa^+(\phi+\phi)]$$

$$\left.\mp \cot\left(\frac{\pi-(\phi+\phi')}{2n}\right)F[kLa^-(\phi+\phi')]\right\} \qquad (4\text{-}18)$$

and the upper sign applies to the soft boundary condition. Hence

$$F(x) = 2j|\sqrt{x}|e^{-jx}\int_{|\sqrt{x}|}^{\infty} e^{-j\tau^2}\,d\tau$$

is the transition function and involves a Fresnel integral. Also

$$a^{\pm}(x) = 2\cos^2\frac{2n\pi N^{\pm}-x}{2}$$

in which $N^{\pm}$ are integers which most nearly satisfy the equations:

$$2\pi nN^+ - x = \pi$$

$$2\pi nN^- - x = -\pi$$

The distance parameter (L) is given in general for a straight wedge by [6]

$$L = \frac{s(\rho_e^i+s)\rho_1^i\rho_2^i\sin^2\beta_o}{\rho_e^i(\rho_1^i+s)(\rho_2^i+s)} \qquad (4\text{-}19)$$

where ρ_e^i is the radius of curvature of the incident wavefront at Q_E taken in the plane containing the incident ray and the unit vector tangent to the edge at Q_E,

ρ_1^i, ρ_2^i are the principal radii of curvature of the incident wavefront.

For the two-dimensional reflected-diffracted case considered here (see Figure 4-8a) the following specific values and equations are used:

$$n = 2 \quad , \qquad \phi_o = 90^\circ$$

$$s = D3 \quad , \qquad \rho_e^i = D1 + D2$$

$$\rho_2^i = D1 + D2$$

$$\rho_1^i = D2 + \frac{D1 \cdot R1 \cdot \cos\phi^i}{2 \cdot R1 + R1 \cdot \cos\phi^i}$$

where R_1 is the radius of curvature of the sinusoidal surface and is given in Equation (4-15).

The total reflected-diffracted field is then the summation of fields coming from all the specular points:

$$\vec{E}^d(s) = \sum_{n=1}^{N} \vec{E}_n^i(Q_E) \cdot D_n \frac{e^{-jks}}{s} \qquad (4\text{-}20)$$

By the theorem of reciprocity, the ray that travels in the reverse direction as shown in Figure 4-8b will produce the same voltage at the receiver terminal as that calculated for Figure 4-8a. Hence the received field is twice the value given by Equation (4-20). All received fields should also be multiplied by the antenna pattern function.

The diffracted field, as shown in Figure 4-9 can also be calculated by Equations (4-17), (4-18), and (4-19). The appropriate parameters for this case (Figure 4-9) are

$$\rho_2^i = D3, \quad \rho_1^i = D3, \quad \rho_e^i = D3$$

so that the distance parameter becomes $L = D3/2$.

(vii) Results

Before showing the computer calculated results of the scattered field, it is enlightening to examine the location of the specular point on the sinusoidal surface for various antenna positions. If the height of the surface is set to zero, there is only one reflection point which is located at the intersection of the flat plate and surface (see Figure 4-10). This solution is independent of the source position. Note, however, that if the corner angle is not a right angle ($\alpha \neq 90$), the reflection point will not be at the intersection, and will depend on the source position.

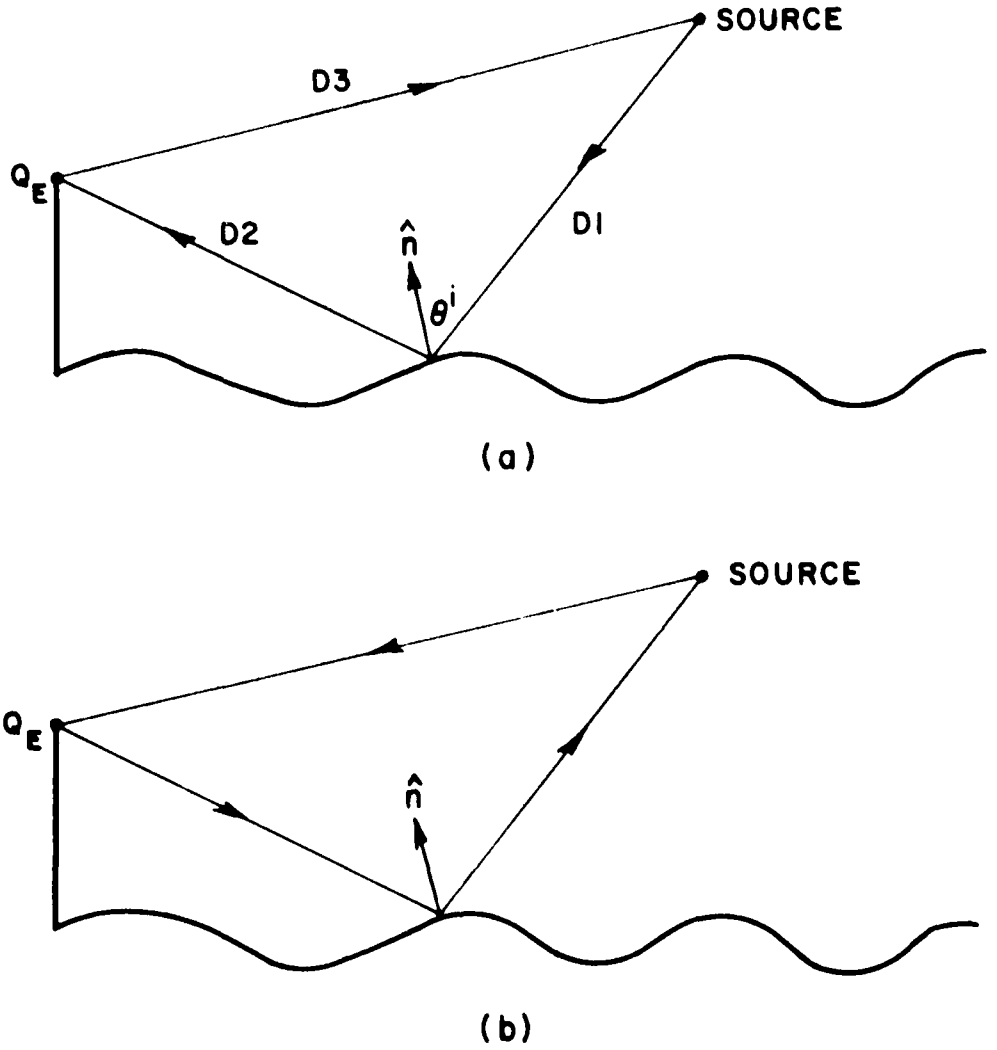

Figure 4-8. Reflected-diffracted rays.

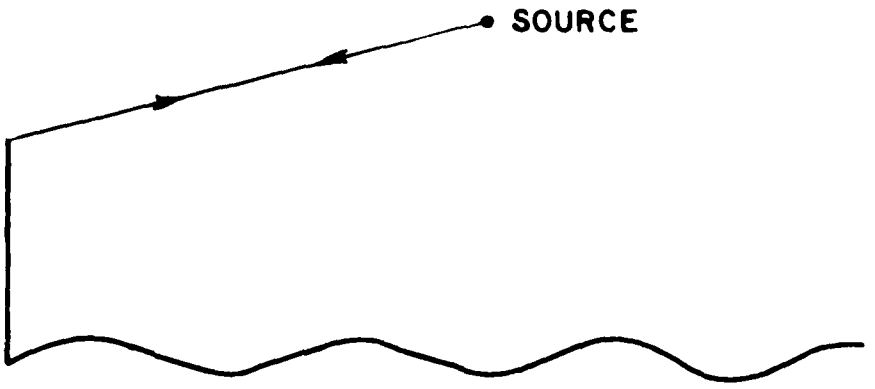

Figure 4-9. Direct diffracted field.

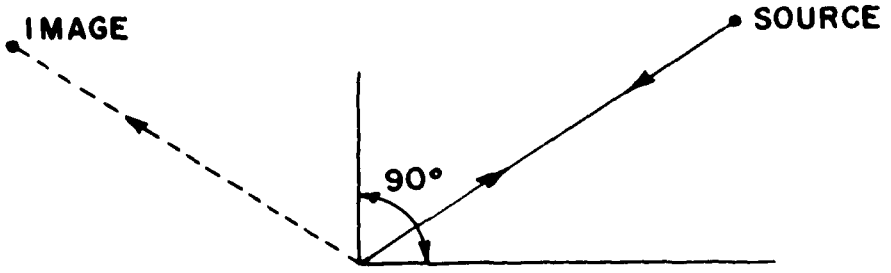

Figure 4-10. Reflection point for μ=90°.

As the amplitude of the sinusoidal surface increases, the number of reflection points also increases. To illustrate this effect, a set of specular point results are shown in Figure 4-11 as the antenna moves along the trajectory shown in Figure 4-4. It is observed (Figure 4-11c) that the number of reflection points is reduced when the source is moved closer to the vertical plate.

For the configuration shown in Figure 4-4 with α 60°, horizontal polarization, and a 15-degree antenna beam, the received signal waveforms are shown in Figure 4-12. Figure 4-12a shows the signature of the corner, i.e., the double bounce reflection alone. The signature of the double bounce reflection plus all diffraction terms is shown in Figure 4-12b. Figure 4-12c gives the measured data from Encounter Simulation Laboratory (ESL). The difference between Figures 4-12b and 4-12c in the region 0·NT·60 is due primarily to back scatter from the small scale structure of the surface.

The GTD received signal waveform of the model shown in Figure 4-4 with angle α equal to 30° is shown in Figure 4-13. In this figure, the calculated result is again compared with the measured waveform taken at the Encounter Simulation Laboratory.

All the above calculations and measurements have included a range-gate function. This range rate requires that each contribution to the received field be multiplied by a function of the distance traveled by the field between the source and the receiver. That is, each term in Equations (4-16) and (4-20) is multiplied by the range gate function. Two types of fields that are back-scattered directly from the sinusoidal surface have not been included in the GTD results. One is the field directly reflected by the sinusoidal surface alone; however, it is not difficult to include this term if it is desired to show the gravity wave contribution to the signature. For example, Figure 4-14 shows the signature for α 60 when the geometrical optics (bright spot) contributions from the large scale gravity waves are included. The other is the back scattering due to the small scale structure (Bragg scatter) on the surface. The GTD method, at the present stage, is not able to analyze the Bragg-type scattering.

The GTD model is employed here only to verify its validity by comparison with the physical optics model which was discussed in section IV-ii. By comparing a number of signatures calculated by each method, it is clear that excellent agreement is obtained between the two approaches for the interaction field waveforms (i.e., the doubly reflected, reflect-diffracted, and diffracted).

(a) sine wave amplitude 1.5"

(b) sine wave amplitude 3.5"

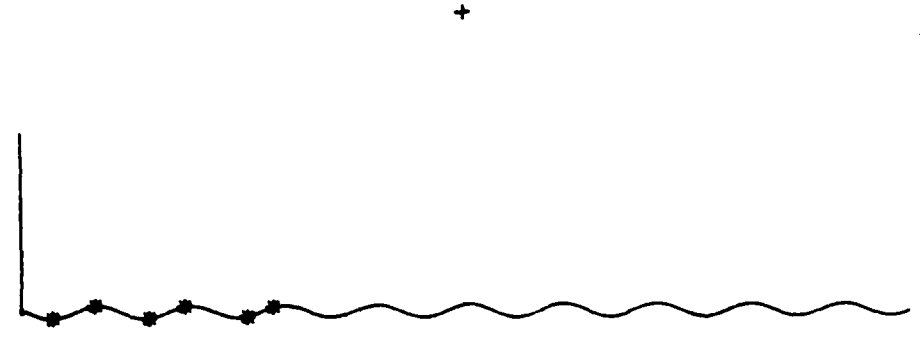

(c) sine wave amplitude 3.5"

Figure 4-11. Specular points for double reflections. (All dimensions not specified here are shown in Figure 1.) Source position indicated by + sign.

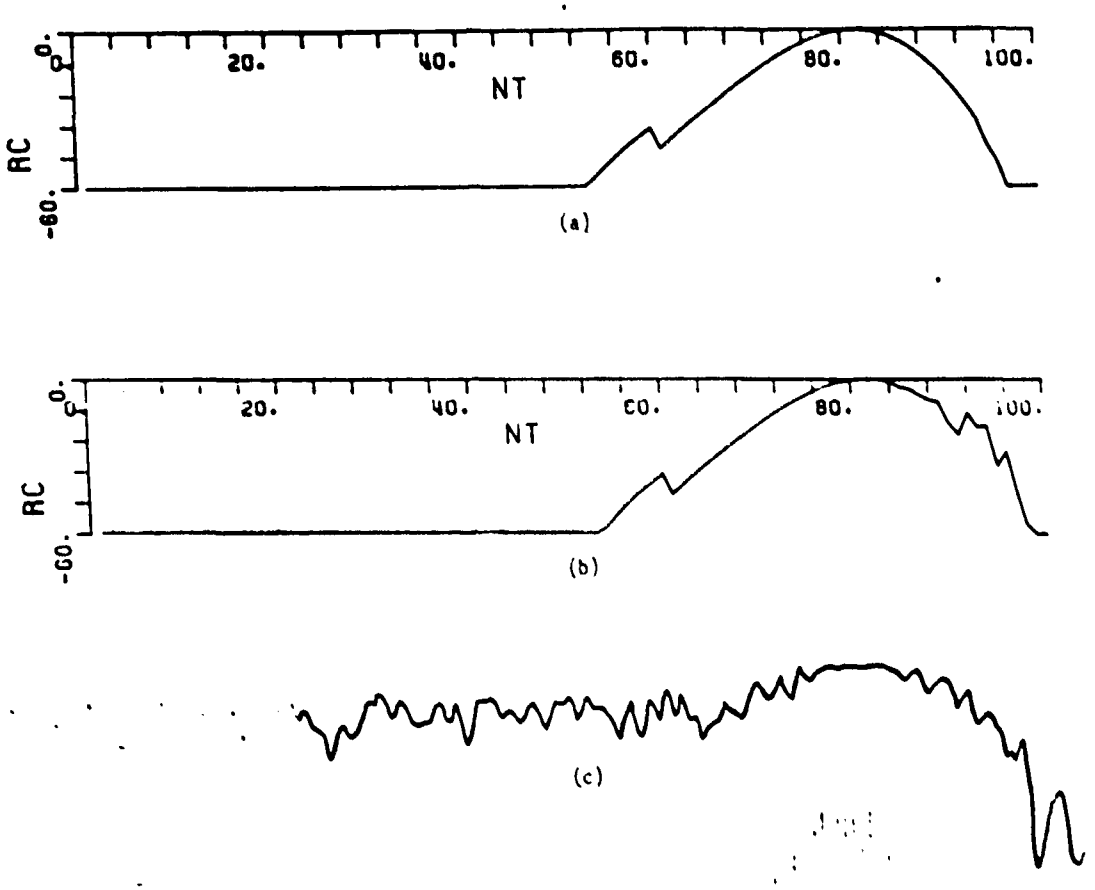

Figure 4-12. GTD signature for α=60°. (a) calculated signature with no diffraction. (b) calculated signature with diffraction. (c) measured data from LSL (Run No. 38). Dive angle ψ=0. Corner angle μ=0.

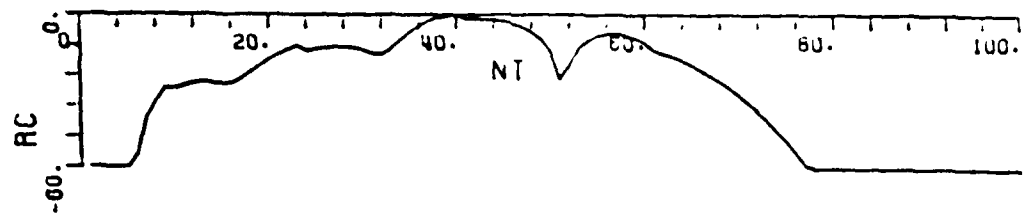

(a)

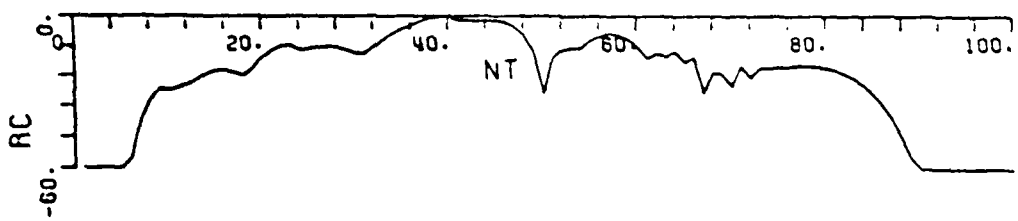

(b)

(c)

Figure 4-13. GTD signature for α=30°. (a) calculated signature with no diffraction. (b) calculated signature with diffraction. (c) measured data from ESL (Run No. 36). Dive angle ψ=0. Corner angle μ= 0.

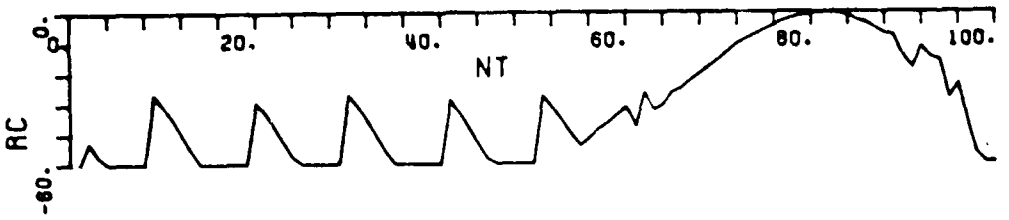

Figure 4-14. GTD calculation of signature including the direct reflection from the sinusoidal surface for the same geometry as Figure 4-12.

V. THE 3-DIMENSIONAL SIMPLIFIED SHIP SEA MODEL

(i) Introduction

In this section we begin the consideration of a more realistic ship-sea model. Although at the present time the structure used to represent the ship is relatively simple, the model has the potential of handling considerably more complex structures without any fundamental change in the computational process.

Here the radar system is represented by a transmit/receive antenna of specified pattern which moves along a specified trajectory. The ship is modelled by a single elliptic cylinder (see Figure 5-1), and the sea is represented by the flat patch model, that is, by a flat surface with specified bi-static scattering behavior. Because our interest is in radar wavelengths much smaller than the characteristic dimensions of the ship, and in trajectories which transit at relatively short range, the problem is formulated here in terms of the geometrical theory of diffraction. The basic geometry is shown in Figure 5-2, in which the antenna is traveling in an arbitrary direction $\hat{A}$ with its main beam axis (bore-sight) pointed in the direction $\hat{B}$ and is illuminating the sea surface over an effective area of W x L. This effective area, which is dependent on the transmitting antenna pattern, is broken up into smaller sub-areas. The scattering from each sub-area is entered into the GTD program as a polarization dependent scattering matrix with scattering coefficients referred to the center of the sub-area. The scattered field from each sub-area of the sea, then, appears to be generated by a new source which in turn illuminates the metallic cylinder, and from which it is reflected to the receiver. The first objective is to compute this doubly reflected field (the ship-sea interaction term), because it represents the major contribution to the overall target signature. Since the elliptical cylinder is a three dimensional structure, a 3-D analysis is necessary. In addition, a near-field analysis is still required since the antenna may be in the near field of the cylinder at the ranges of interest.

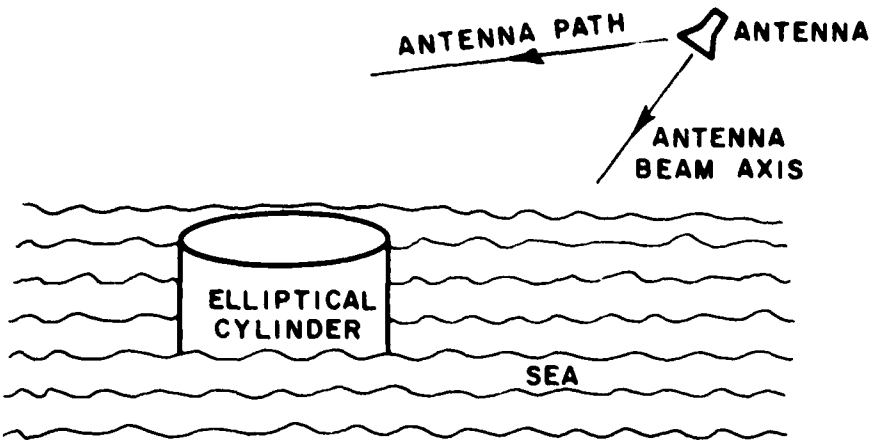

Figure 5-1. Simplified ship model at sea.

(ii) Antenna Pattern and Field Incident Upon the Sea Surface

The antenna is taken to be a plane rectangular sheet of current with coordinate system as shown in Figure 5-3. Although a near-field analysis is required to specify the range dependence of the radiated field, it has been found that the angular dependence can be approximated simply by the far field pattern function of the source.

The radiated far zone electric fields in spherical coordinates are given by [8]

$$E_\theta = \frac{j\omega\mu}{4\pi r} e^{-jkr} \int_{-L/2}^{L/2} \int_{-W/2}^{W/2} [\sin\theta J_z(x',z') - \cos\theta\cos\phi J_x(x',z')]$$

$$\cdot\, e^{jk(x'\sin\theta\cos\phi + z'\cos\theta)} dx'\, dz' \qquad (5\text{-}1a)$$

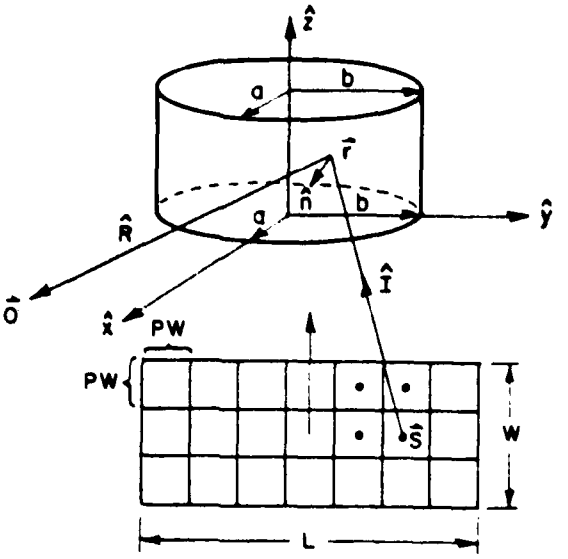

(a) PERSPECTIVE TOP VIEW

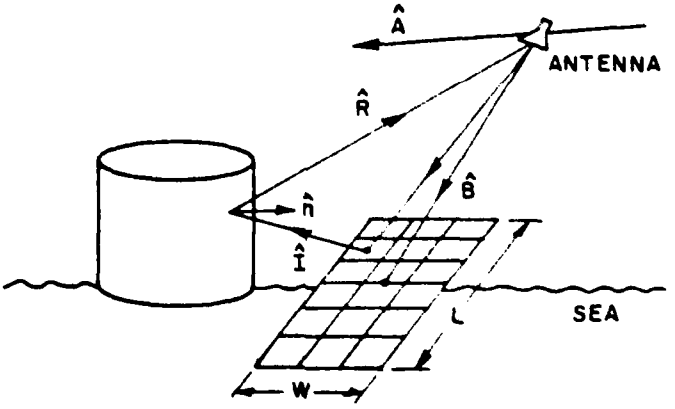

(b) PERSPECTIVE SIDE VIEW

Figure 5-2. Geometry of the cylinder-flat patch model.

$$E_\phi = \frac{j\omega\mu}{4\pi r} \sin\phi \, e^{jkr} \int_{-L/2}^{L/2} \int_{-W/2}^{W/2} J_x(x',z') e^{jk(x'\sin\theta\cos\phi + z'\cos\theta)} dx'dz' \tag{5-1b}$$

One must note that the x-y-z coordinate system specified in Figure 5-3 is independent of that specified in section IV.

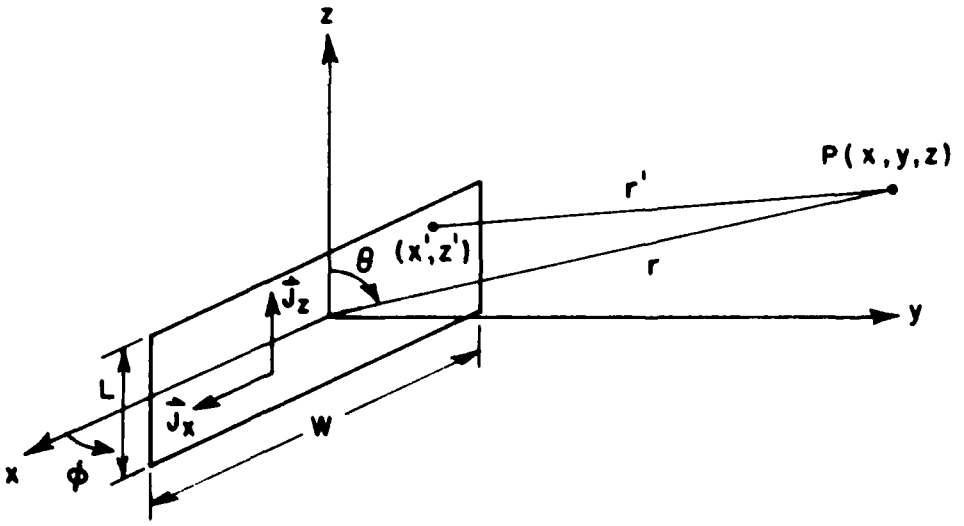

Figure 5-3. Source coordinate system.

Although the aperture distribution and corresponding antenna pattern may have any form, for convenience we have assumed that the aperture current distribution is z-directed and gaussian, given by [8]

$$J_z(x',z') = e^{-\pi\left(\frac{x'}{a}\right)^2} \cdot e^{-\pi\left(\frac{z'}{a}\right)^2}$$

$$J_x = 0$$

where a is a constant parameter which determines the beam width.

Since the gaussian source function is diminishingly small outside the limits of integration, the integrals can be approximated by letting the limits of integration go to infinity, with the result that

$$E_\theta = \frac{j\omega\mu}{4\pi r} e^{-jkr} \sin\theta \; e^{-\frac{(ka\cos\theta)^2}{4\pi}} \cdot e^{-\frac{(ka\,\sin\theta\cos\phi)^2}{4\pi}}$$

$$= \frac{j\omega\mu}{4\pi r} e^{-jkr} \sin\theta \; e^{-\frac{(ka)^2}{4\pi}(\cos^2\theta+\sin^2\theta\cos^2\phi)} \qquad (5\text{-}2)$$

$$E_\phi = 0.$$

For an x-directed, gaussian distributed current, the electric fields are given by

$$E_\theta = \frac{-j\omega\mu}{4\pi r} e^{-jkr} \cos\theta\cos\phi \; e^{-\frac{(ka)^2}{4\pi}(\cos^2\theta+\sin^2\theta\cos^2\phi)} \qquad (5\text{-}3a)$$

$$E_\phi = \frac{j\omega\mu}{4\pi r} e^{-jkr} \sin\phi \; e^{-\frac{(ka)^2}{4\pi}(\cos^2\theta+\sin^2\theta\cos^2\phi)} \qquad (5\text{-}3b)$$

Since the antenna generates a 15-degree broadside (θ=90°, ϕ=90°) beam, and $\cos\theta\cdot\cos\phi$ is vanishingly small near the broadside direction, E_θ is negligible for the x polarized source distribution.

To conclude, the fields that are incident upon the sea surface are given by Equations (5-2) and (5-3b) for a vertically (J_z) and horizontally (J_x) polarized antenna, respectively.

(iii) Sea-surface Scattering Characteristic

The scattering characteristics of each sub-area, utilizing the flat patch model, will be determined by the bistatic radar cross-section of the ocean. The complete bi-static cross-section of the ocean, over all possible bi-static angles, has never been measured, so that for the purposes of this report a cross-section based on theoretical considerations must be utilized. Fortunately, because of the geometrical configuration of the problem, the significant ray paths (from antenna to sea surface to ship to antenna) all involve predominantly forward scatter. At microwave frequencies, the specular component of the total scattering cross-section of the ocean is determined by a reflection (i.e., an optical scattering) process controlled by the slope distribution of the surface. Thus, referring to the geometry of Figure 5-4, where the incident ray lies in the y'-z' plane, the radar cross-section per unit area is given by

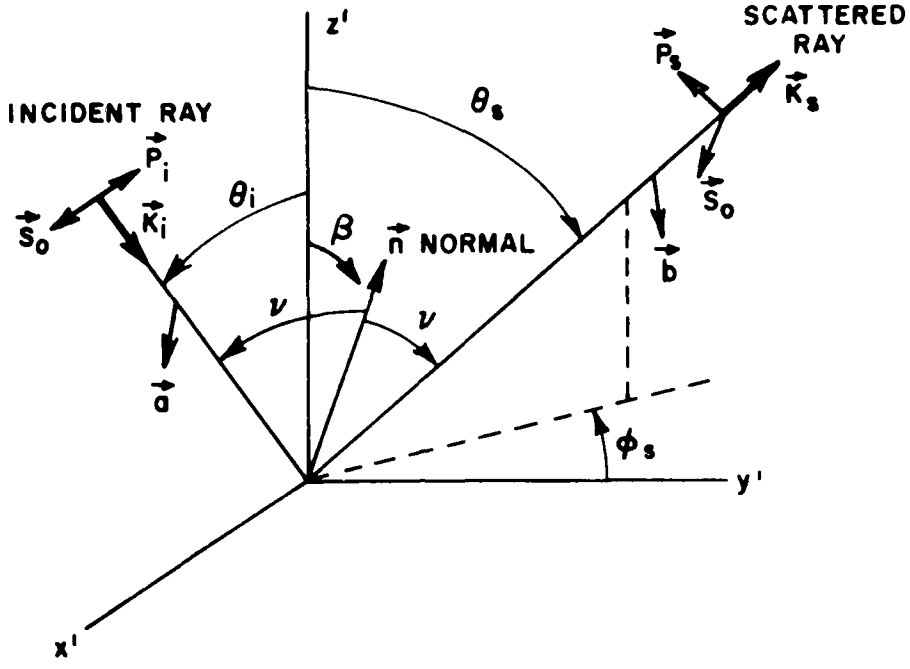

Figure 5-4. Geometry of bistatic cross-section.

$$\sigma_{ij}(\theta_i,\theta_s,\phi_s) = |R_{ij}(\nu)|^2 \pi \sec\theta_i \; p(\beta) \tag{5-4}$$

where R_{ij} is a polarization dependent Fresnel coefficient, and $p(\beta)d\beta$ is the probability that the surface normal $\hat{n}$ makes an angle between β and $\beta+d\beta$ with the vertical. This equation determines the bistatic cross-section for a wave incident from the direction defined by θ_i, into the direction defined by θ_s and ϕ_s. These two directions then define the direction $\hat{n}$ of the surface normal required for specular reflection from θ_i into $\theta_s\phi_s$, and the local angle of incidence ν. The reflection process also transforms the polarization of the incident wave. However it is more convenient to specify the polarization transformation in terms of a specific transmitter state with unit polarization vector $\hat{a}$ (which may be complex, $\hat{a} \cdot \hat{a}^* = 1$) and a specific received polarization state $\hat{b}$, ($\hat{b}\cdot\hat{b}^*=1$). In that case

$$R(\nu) = R_{\perp}(\nu)(\hat{a}\cdot\hat{s})(\hat{b}\cdot\hat{s}) + R_{\parallel}(\nu)(\hat{a}\cdot\hat{p}_i)(\hat{b}\cdot\hat{p}_s) \tag{5-5}$$

where

$$R_{\perp}(\nu) = (\cos\nu - E)/(\cos\nu + E) \tag{5-6}$$

$$R_{\parallel}(\nu) = (\varepsilon\cos\nu - E)/(\varepsilon\cos\nu + E)$$

$$E = (\varepsilon - \sin^2\nu)^{1/2}$$

ε = complex dielectric constant of sea water

$$\hat{s} = (\hat{k}_i \times \hat{k}_s)/\sin 2\nu$$

$$\hat{p}_i = \hat{s} \times \hat{k}_i$$

$$\hat{p}_s = \hat{s} \times k_s$$

The angles ν and δ are found from

$$\cos 2\nu = \cos\theta_i\cos\theta_s - \sin\theta_i\sin\theta_s\cos\phi_s \tag{5-7}$$

$$\cos\delta = (\cos\theta_s + \cos\theta_i)/2\cos\nu \tag{5-8}$$

The probability density $p(\delta)$ for the surface slope distribution depends on a number of oceanographic variables, but for the purposes of this report is assumed to have the simple isotropic form

$$p(\delta) = \frac{\cos\delta}{\pi s^2} \exp(-\tan^2\delta/s^2(1+2s^2)) \tag{5-9}$$

s = mean square surface slope.

Thus, apart from an unknown phase the effect of a patch sea is that of a polarization and amplitude transforming reflection of the incident ray into a ray in the "reflected" direction.

(iv) Numerical Search Technique for Points of Reflection

Once the "reflecting" properties of the patch of ocean are known, we may return to the problem of calculating the double-bounce contribution of a particular patch. From any one of the sub-areas to the receiver via the reflection from the elliptical cylinder, there must exist one reflection point on the cylinder except when the receiver is in the shadow region of the cylinder. To find this reflection point, the laws of reflection, as defined by Equations (4-6) and (4-7) must

be satisfied. When these laws are applied in a systematic manner, it is found [9] that the position of the reflection point can be recovered from a single unknown parameter α (to be defined later) which satisfies a sixth order polynomial,

$$C_6\alpha^6+C_5\alpha^5+C_4\alpha^4+C_3\alpha^3+C_2\alpha^2+C_1\alpha^1+C_0 = 0 \qquad (5\text{-}10)$$

The coefficients C_0, C_1, etc. are functions of the source location, receiver location, and cylinder parameters. Since the derivation of this polynomial is quite a laborious process, and it has been derived in the reference given above, it will not be derived again here.

The polynomial technique is very time consuming if it must be carried out for every sub-area at each point of the trajectory. Hence it is used only for initial acquisition of the reflection point for the first sub-area of the Nth row (A_{N1}) as shown in Figure 5-5. This reflection point is then tracked by a very fast numerical search technique through many small increments (width=Δv) to the new reflection point for sub-area A_{N2}. This numerical search technique is thereafter applied to find all the reflection points for the sub-areas in the same row (sub-areas A_{N3}, A_{N4}, etc.), and this procedure is repeated for each row.

The polynomial method can be considered as an exact solution (except for a numerical truncation error). In the numerical search technique, a new reflection point is found from the previously determined reflection point; therefore this approach can have an accumulation of errors. In order to control this accumulation of errors, an error bound is defined such that if it is exceeded by the accumulated error, the number of increments is increased (Δv being reduced) until the error bound is satisfied. The numerical search technique is briefly discussed below. We first define (see Figure 5-2) position vectors $\hat{s}$, $\hat{o}$, and $\hat{r}$, where the vector $\hat{s}$ is the position of the center of sub-area, vector $\hat{o}$ is the position of observation point which is fixed for any instantaneous antenna location, and vector $\hat{r}$ is the position of reflection point on the cylinder. Thus,

$$\hat{s} = x_s\hat{x} + y_s\hat{y}$$

$$\hat{o} = x_o\hat{x} + y_o\hat{y} + z_o\hat{z}$$

$$\hat{r} = x_r\hat{x} + y_r\hat{y} + z_r\hat{z}.$$

A parameter v is introduced to define the reflection point on the elliptical cylinder such that

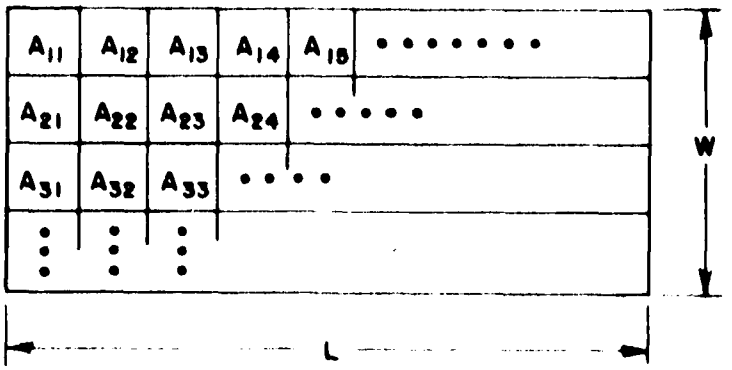

(a)

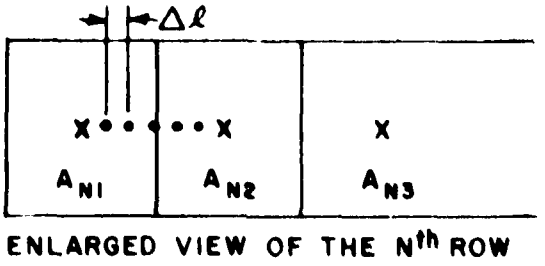

(b)

Figure 5-5. Sub-divided patches of the illuminated sea surface.

$$\cos v = \frac{x_r}{a}, \qquad \sin v = \frac{y_r}{b}$$

where a, b are the semi-major and semi-minor axes of the ellipse. Thus,

$$\vec{r} = a \cos v\, \hat{x} + b \sin v\, \hat{y} + z_r\, \hat{z} .$$

Now Equations (4-6) and (4-7) can be combined to form:

$$(\hat{n}\cdot\hat{l})(\hat{n}\times R) + (\hat{n}\times\hat{l})(\hat{n}\cdot\vec{R}) = 0 \qquad (5\text{-}11)$$

where

$$\vec{n} = n_x\hat{x} + n_y\hat{y} = b\cos v\,\hat{z} + a\sin v\hat{y} \cdots \text{normal vector} \qquad (5\text{-}12a)$$

$$\vec{I} = I_x\hat{x} + I_y\hat{y} + I_z z = \vec{r} - \vec{s}$$
$$= (a\cos v - x_s)\hat{x} + (b\sin v - y_s)\hat{y} + z_r\hat{z} \cdots \text{incident vector} \qquad (5\text{-}12b)$$

$$\vec{R} = R_x\hat{x} + R_y\hat{y} + R_z\hat{z} = \vec{0} - \vec{r}$$
$$= (x_o - a\cos v)x + (y_o - b\sin v)\hat{y} + (z_o - z_r)\hat{z} \cdots \text{reflection vector} \qquad (5\text{-}12c)$$

After performing the dot and cross products, Equation (5-11) can be separated into two equations:

$$f(v,x_s,y_s) = (n_xI_x+n_yI_y)(n_xR_y-n_yR_x) + (n_xR_x+n_yR_y)(n_xI_y-n_yI_x) = 0 \qquad (5\text{-}13a)$$

$$g(v,x_s,y_s,z_r) = (n_xI_x+n_yI_y)R_z + (n_xR_x+n_yR_y)I_z = 0 \qquad (5\text{-}13b)$$

By substituting Equations (5-12b) and (5-12c) into Equation (5-13b), one finds that

$$z_r = \frac{(n_xI_x + n_yI_y)z_o}{(n_xI_x+n_yI_y)-(n_xR_x+n_yR_y)} \qquad (5\text{-}14)$$

which is a function of v, x_s and y_s. For Equation (5-13a), one can apply a technique similar to that discussed in section 4 to obtain

$$f_{j+1} = f_j + \delta f_j = 0$$

where

$$\delta f_j \cong \frac{\partial f_j}{\partial v}\delta v + \frac{\partial f_j}{\partial x_s}\delta x_s + \frac{\partial f_j}{\partial y_s}\delta y_s.$$

Hence,

$$\delta v = - \frac{f_j + (\partial f_j/\partial x_s)\delta x_s + (\partial f_j/\partial y_s)\delta y_s}{\partial f_j/\partial v} \qquad (5\text{-}15)$$

which is a function of the old reflection point (v, x_s, y_s) and the incremental distances $(\delta x_s, \delta y_s)$. The new reflection point in the x-y plane is now defined by $v_{j+1} = v_j + \delta v$ and can be substituted along with the new source location $(x_s + \delta x_s, \delta y_s + y_s)$ into Equation (5-14) to yield the new reflection point in the z-coordinate. After the new point (j+1) has been determined, it can be substituted into Equations (5-15) and (5-14) again to find the next new point (j+2). This process continues until it reaches the center of the adjacent sub-area from which an additional reflected field is then calculated.

(v) Reflection from the Elliptical Cylinder

Once the field scattered from the center of each sub-area has been calculated and the corresponding reflection point on the cylinder located, the reflected field incident on the receiver is readily computed using the geometry illustrated in Figure 5-6. The scattered field for each sub-area, as described in section V-iii, is treated as the field incident on the cylinder. The reflected field is given by

$$\dot{E}^r(s) = \dot{E}^i(Q_R) \cdot \bar{\bar{R}} \sqrt{\frac{\rho_1^r \rho_2^r}{(\rho_1^r + s)(\rho_2^r + s)}}\; e^{-jks}$$

where

$\dot{E}^i(Q_R)$ is the 'incident' field at the reflection point Q_R,

S is the distance between reflection point and observation point, and

ρ_1^r, ρ_2^r are principal radii of curvature of the reflected wavefront at the point of reflection, namely

$$\frac{1}{\rho_{1,2}^r} = \frac{1}{S'} + \frac{1}{\cos\theta^i}\left[\frac{\sin^2\theta_2}{R_1} + \frac{\sin^2\theta_1}{R_2}\right] \pm \sqrt{\frac{1}{\cos^2\theta^i}\left[\frac{\sin^2\theta_2}{R_1} + \frac{\sin^2\theta_1}{R_2}\right]^2 - \frac{4}{R_1 R_2}}$$

where

S' is the distance between source and reflection point,

θ^i is the angle of incidence with $\cos\theta^i = \hat{n}\cdot\hat{R} = -\hat{n}\cdot\hat{I}$,

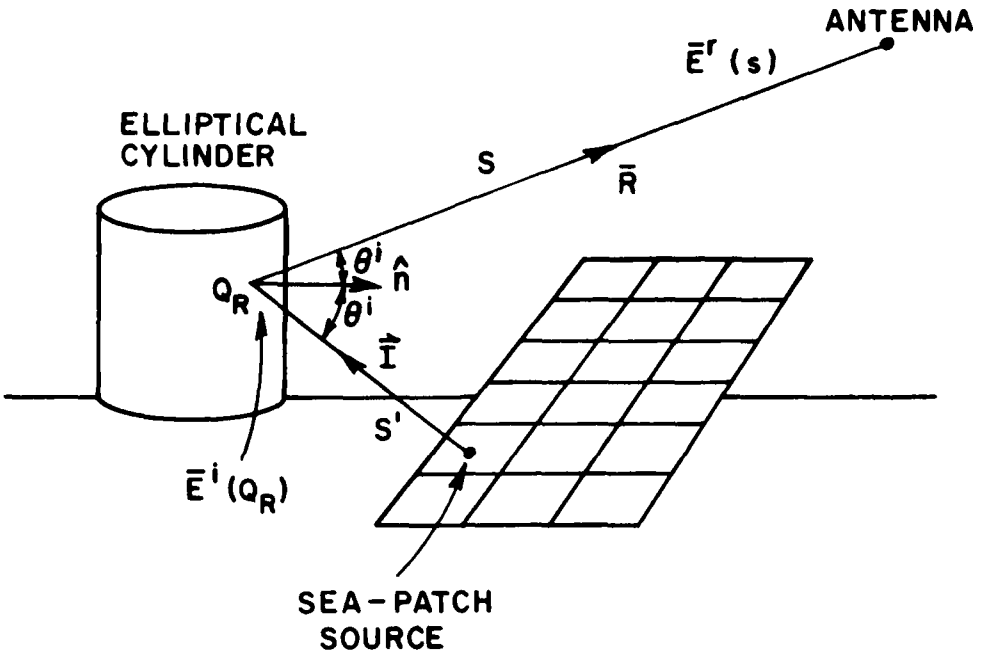

Figure 5-6. Geometry for field reflected from cylinder.

θ_1 is the angle between the incident ray and the tangent vector (e_1) to the cylinder in the x-y plane at the reflection point, (see Figure 5-7)

θ_2 is the angle between the incident ray and the tangent vector (e_2) in the z-plane (see Figure 5-7)

R_1 and R_2 are the radii of curvature of the elliptical cylinder,

$$R_2 = \infty; \quad R_1 = \frac{(b^2\cos^2 v + a^2\sin^2 v)^{3/2}}{ab} .$$

Using the above expressions, one finds that

$$\frac{1}{\rho_1^r} = \frac{1}{S^r} + \frac{2\sin^2\theta_2}{R_1\cos\theta^i} \quad \text{and} \quad \frac{1}{\rho_2^r} = \frac{1}{S^r}$$

$\bar{\bar{R}}$ is the dyadic reflection coefficient given by

$$\bar{\bar{R}} = [\hat{e}_{\parallel}^{i}\hat{e}_{\parallel}^{r} - \hat{e}_{\perp}\hat{e}_{\perp}] \qquad (5\text{-}16)$$

where $\hat{e}_{\perp}$ is unit vector perpendicular to the plane of incidence (see Figure 5-7) and $\hat{e}_{\parallel}^{i}$, $\hat{e}_{\parallel}^{r}$ are unit vectors parallel to the plane of incidence and reflection, respectively.

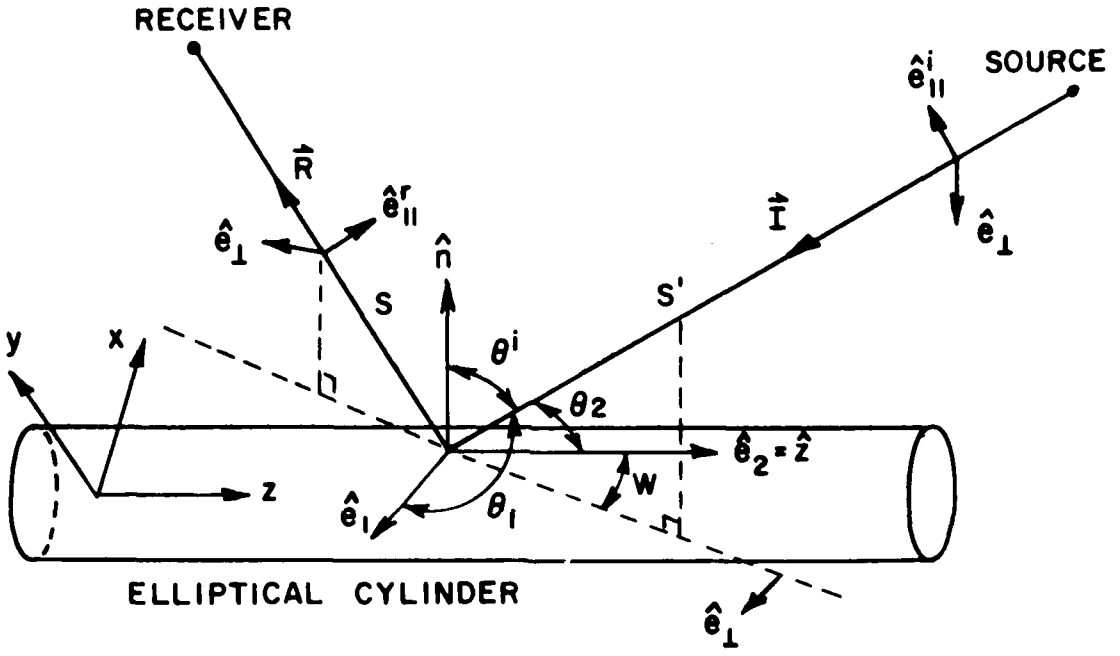

Figure 5-7. Reflection coordinate transformation system on the cylinder.

The incident vector $\hat{I}$ in Figure 5-7 can be transformed to the orthogonal coordinate system $\hat{n}$, $\hat{e}_1$, $\hat{e}_2$ as

$$\hat{I} = -\cos\theta^{i}\hat{n} - \sin\theta^{i}\cos\omega\,\hat{e}_2 - \sin\theta^{i}\sin\omega\,\hat{e}_1 \qquad (5\text{-}17)$$

where ω is the angle between $\hat{e}_2$ and the projection of $\hat{I}$ onto the plane containing $\hat{e}_1$ and $\hat{e}_2$ such that

$$\hat{I} \cdot \hat{e}_2 = -\sin\theta^{i}\cos\omega \ .$$

Since it is also true that $\hat{I} \cdot \hat{e}_2 = -\cos\theta_2$, we have

$$\cos\omega = \frac{\cos\theta_2}{\sin\theta^i} \quad .$$

The unit vector $\hat{e}_1$ is found by the orthogonal relationship:

$$\hat{e}_1 = \hat{e}_2 \times \frac{\vec{n}}{|\vec{n}|} = \hat{z} \times \frac{\vec{n}}{|\vec{n}|}$$

where $\vec{n}$ can be obtained from Equation (5-12a). Hence

$$\hat{e}_1 = e_{1x}\hat{x} + e_{1y}\hat{y}$$

with

$$e_{1x} = -\frac{a \sin v}{\sqrt{b^2\cos^2 v + a^2\sin^2 v}} \quad \text{and} \quad e_{1y} = \frac{b \cos v}{\sqrt{b^2\cos^2 v + a^2\sin^2 v}}$$

From Figure 5-7 one can easily transform the vectors used in the dyadic reflection coefficient into the x-y-z coordinate system,

$$\hat{e}_\perp = -\sin\omega\, \hat{e}_2 + \cos\omega\, \hat{e}_1$$

$$= -\sin\omega\, \hat{z} + \cos\omega \cdot e_{1x}\, \hat{x} + \cos\omega \cdot e_{1y}\hat{y} \qquad (5\text{-}18a)$$

and

$$\hat{e}^i_{\shortparallel} = \hat{I} \times \hat{e}_\perp \qquad (5\text{-}18b)$$

$$\hat{e}^r_{\shortparallel} = \hat{R} \times \hat{e}_\perp \qquad (5\text{-}18c)$$

(vi) Summary of Solutions and Results

For each sub-area of the sea surface scattering matrix, the field incident upon it is calculated from the antenna's radiation functions as expressed in Equations (5-2) and (5-3b). The scattered field from this sub-area is then obtained by multiplying the above incident field by a scattering coefficient which is a function of the angle of incidence, angle of reflection, sea surface characteristics, polarization of the incident field, and size of the sub-area. It is clear that the angle of reflection is determined from the location of the reflection point on the cylinder. This location is first calculated by the polynomial method and then tracked by the numerical search technique as the scattering source moves from one sub-area to another. Once the scattered field from the sub-area to the reflection point on the cylinder is computed, the reflected field from this reflection point to the receiver is readily calculated by the method of GTD which is given by Equation (4-14). The final solution, i.e., the total received field, is then a summation of all the doubly reflected fields for the sub-areas that are illuminated by the antenna.

Presently, a computer program to obtain the reflection points on the elliptical cylinder has been completed and the results verified in terms of hand calculations. As an example, for the case of broadside incidence on the cylinder, as shown in Figure 5-8, the locations of the reflection points on the cylinder versus the sub-area positions are illustrated in Figures 5-9 and 5-10. Figure 5-9 shows the reflection points in the x-y plane as measured by the angle v, and Figure 5-10 shows the reflection points in the z-plane as measured by the height z_r. For the case of off-broadside incidence (45°), shown in Figure 5-11, the reflection points versus the positions of the sub-area are illustrated in Figures 5-12 and 5-13. The curves of position generated for broadside incidence are symmetric with respect to the center sub-area as expected. The curves in Figures 5-9 and 5-10 are nearly straight lines for the reason that the broad face of the elliptical cylinder is nearly flat. The abrupt change at the end of the curves in Figures 5-12 and 5-13 is due to the reason that the reflection points have reached the narrow end of the elliptical cylinder where the surface curvature varies drastically.

At the present time the construction of a computer code to implement this ship-sea model has not been completed. However, a number of preliminary computations have been made. By taking into account only the double bounce corner contribution (forward scatter from transmitter to ocean to ship to receiver), a number of typical signatures for the geometry illustrated in Figure 5-14 have been calculated. In Figures 5-15 through 5-19, typical signatures with horizontal trajectories made with a 15° antenna beam at a depression angle of 60° are shown, for the case of the elliptic cylinder target with semi-major axis of 25 length units and a semi-minor axis of 5 length units. The trajectory altitude is

40.5 length units, and the horizontal range (radar to target center) varies from 0 to 120 units. The parameter in the signature is the approach angle which varies from broadside (SAH=0°) to head-on (SAH=90°). Although the general form of the signatures is quite similar, being strongly influenced by the assumed antenna pattern and range gate, the relative received voltage varies markedly as the approach angle changes.

Although the full implementation of the model remains to be carried out, particularly the introduction of a back-scattering cross-section from each patch (to model the no-target clutter level), it is evident from Figures 4-16 to 4-19 that the model can produce, in a computationally efficient way, realistic signatures for the encounter of a radar system with a ship at sea.

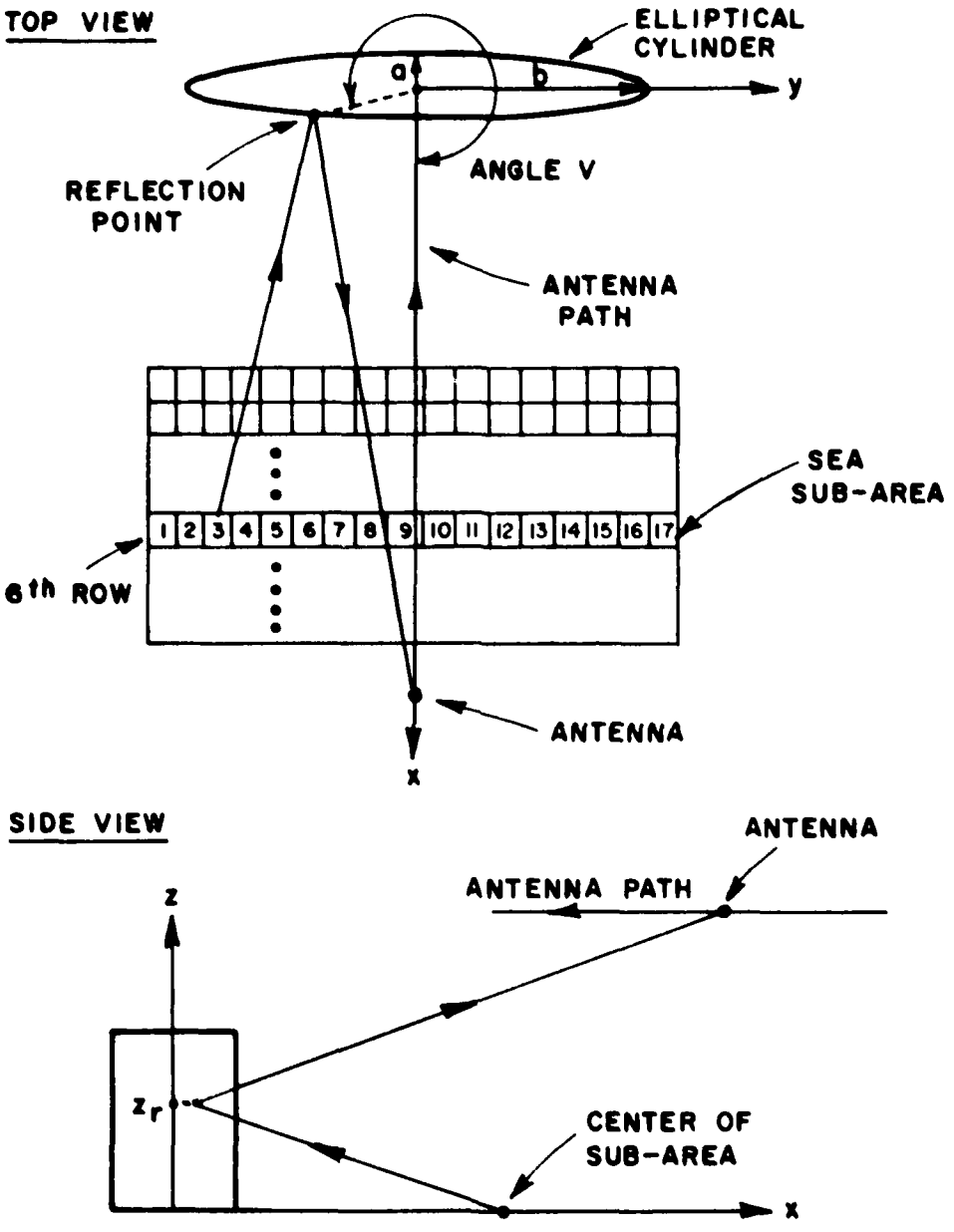

Figure 5-8. Characteristic views of elliptical cylinder and position matrix for broadside incidence. The antenna is instantaneously fixed at location (x=55.2, y=0, z=40.5, and a=3, b=30 arbitrary distance units).

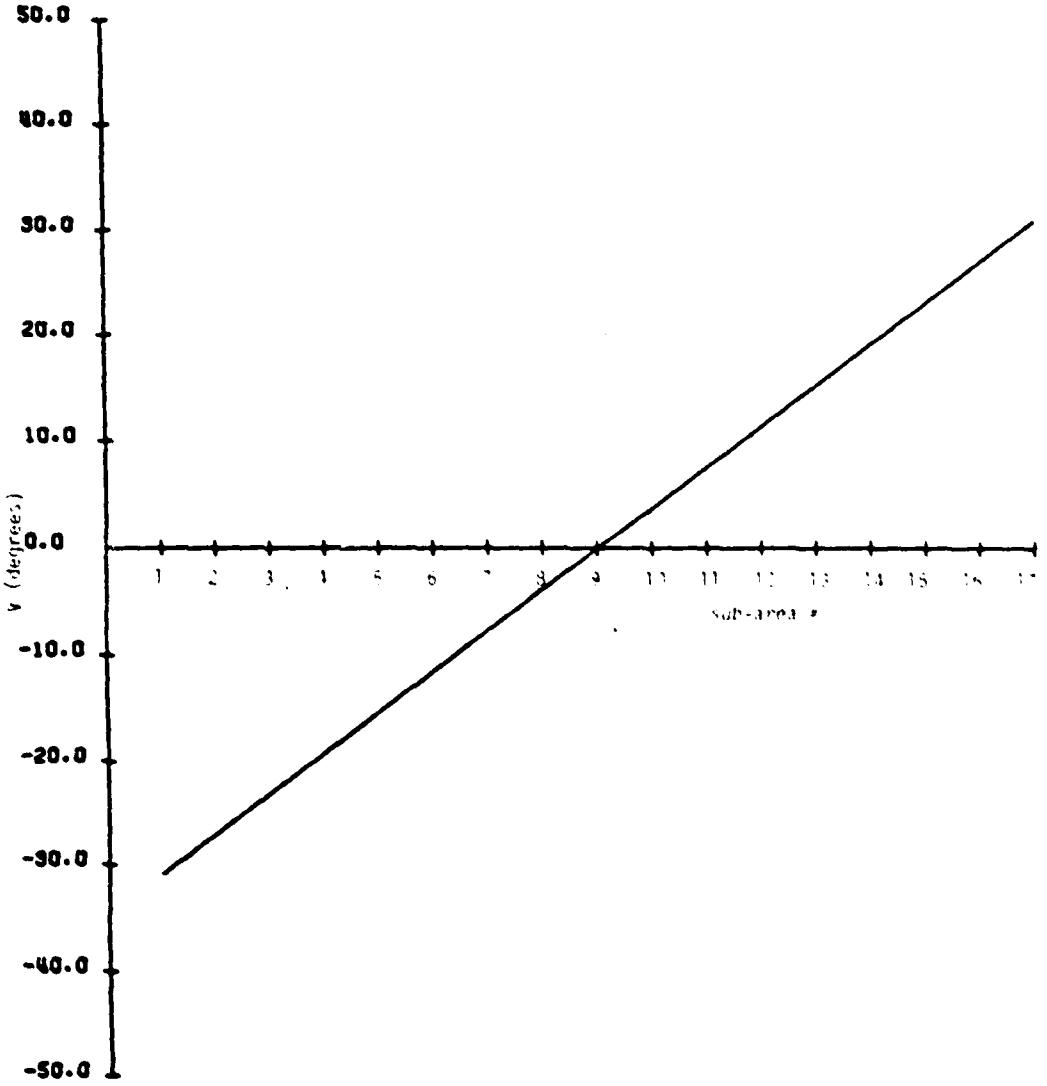

Figure 5-9. Reflection points (measured in angular position V) versus the sub-area location for the case shown in Figure 5-8. The sixth row in the scattering matrix is used.

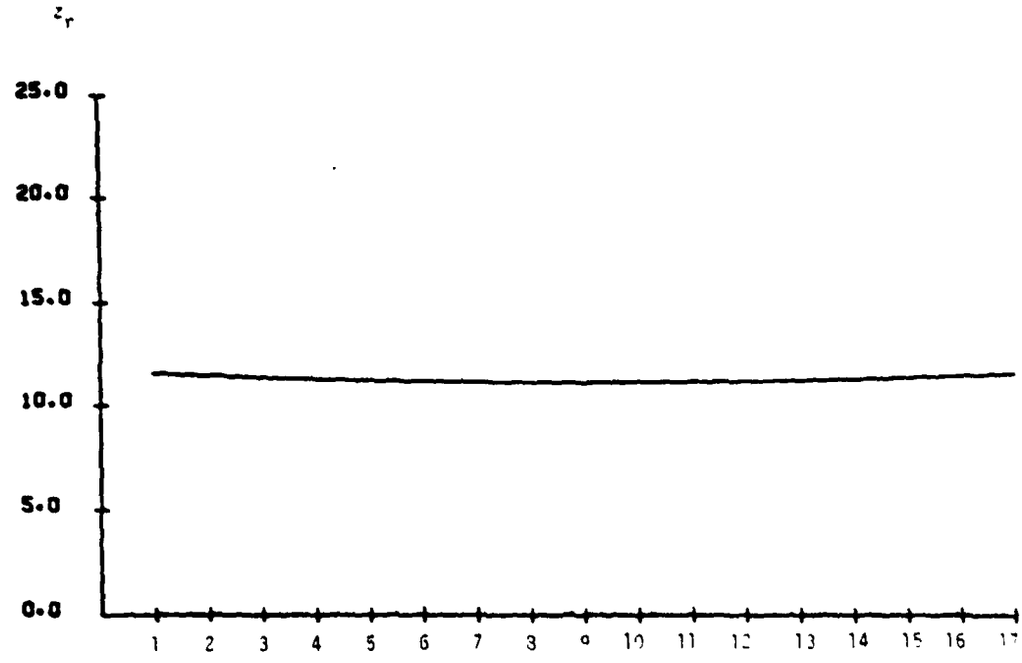

Figure 5-10. Reflection points (measured in vertical height z_r) versus the sub-area location for the same case shown by Figure 5-9.

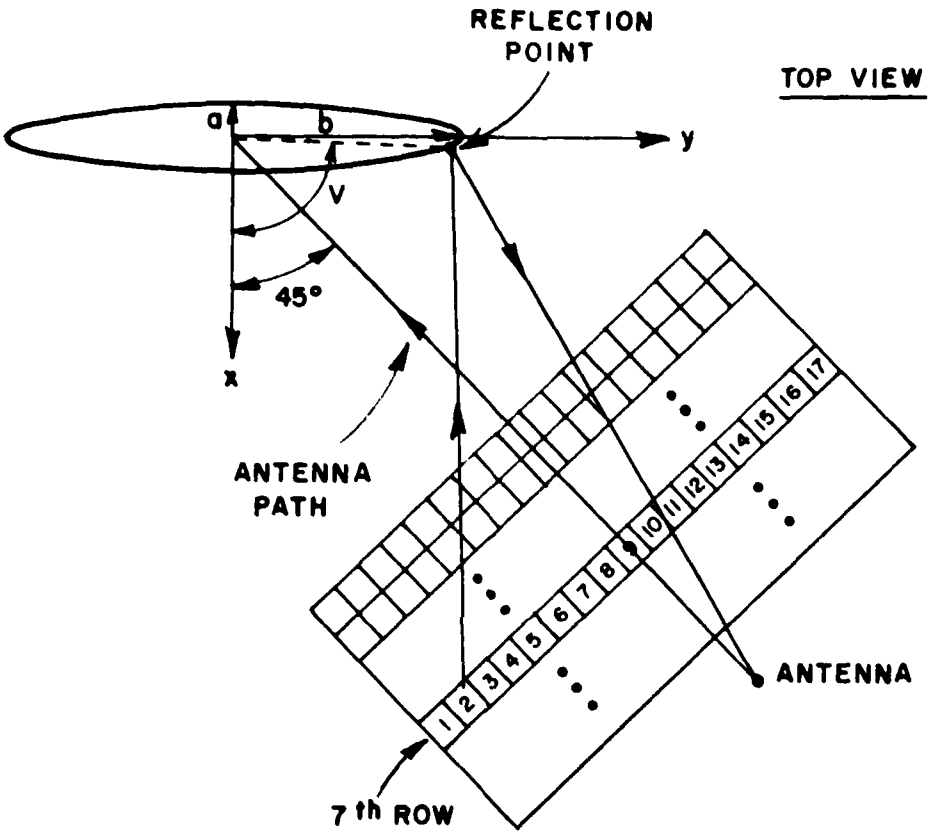

Figure 5-11. Characteristic view of elliptical cylinder and position matrix for off-broadside incidence of the antenna. The antenna is instantaneously fixed at location (x=39.0", y=39.0", z=40.5"0 and a=3", b=30".

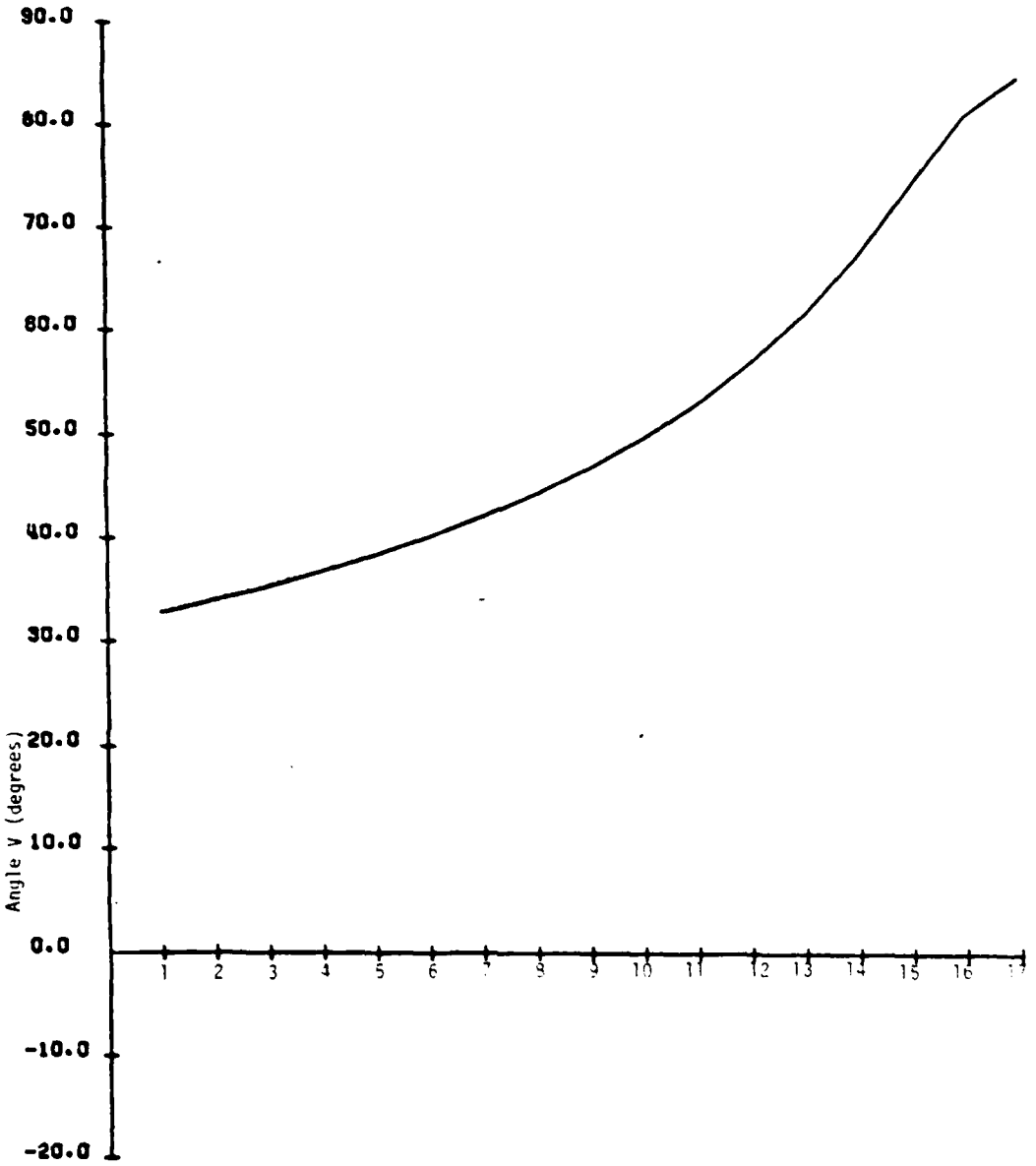

Figure 5-12. Reflection points (measured in angular position V) versus the sub-area location for the case shown in Figure 5-11. The seventh row in the scattering matrix is used.

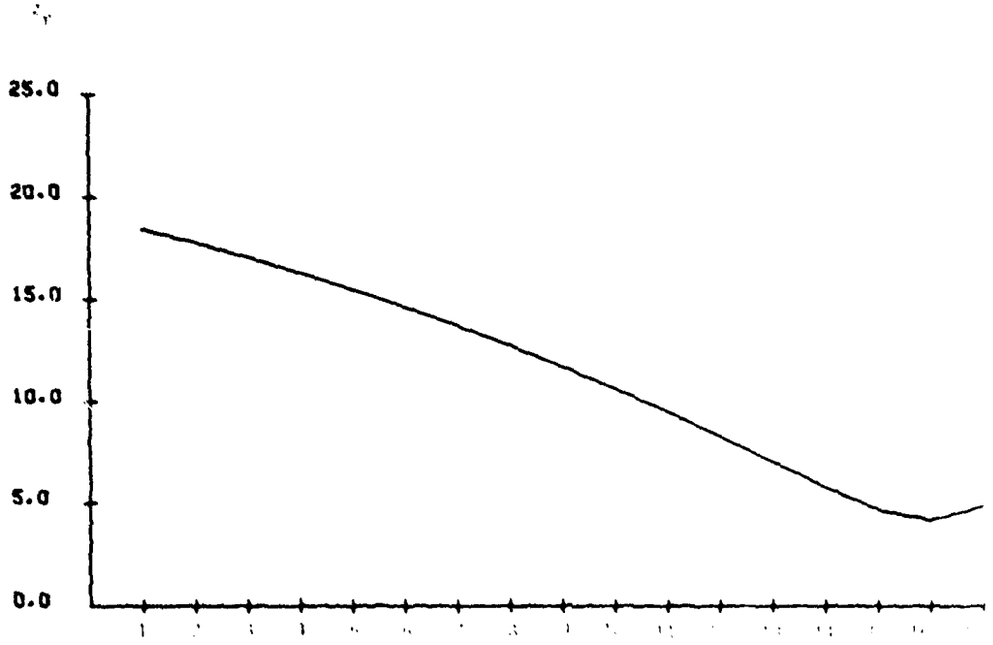

Figure 5-13. Reflection points (measured in vertical height z_r) versus the sub-area locations for the same case shown by Figure 5-12.

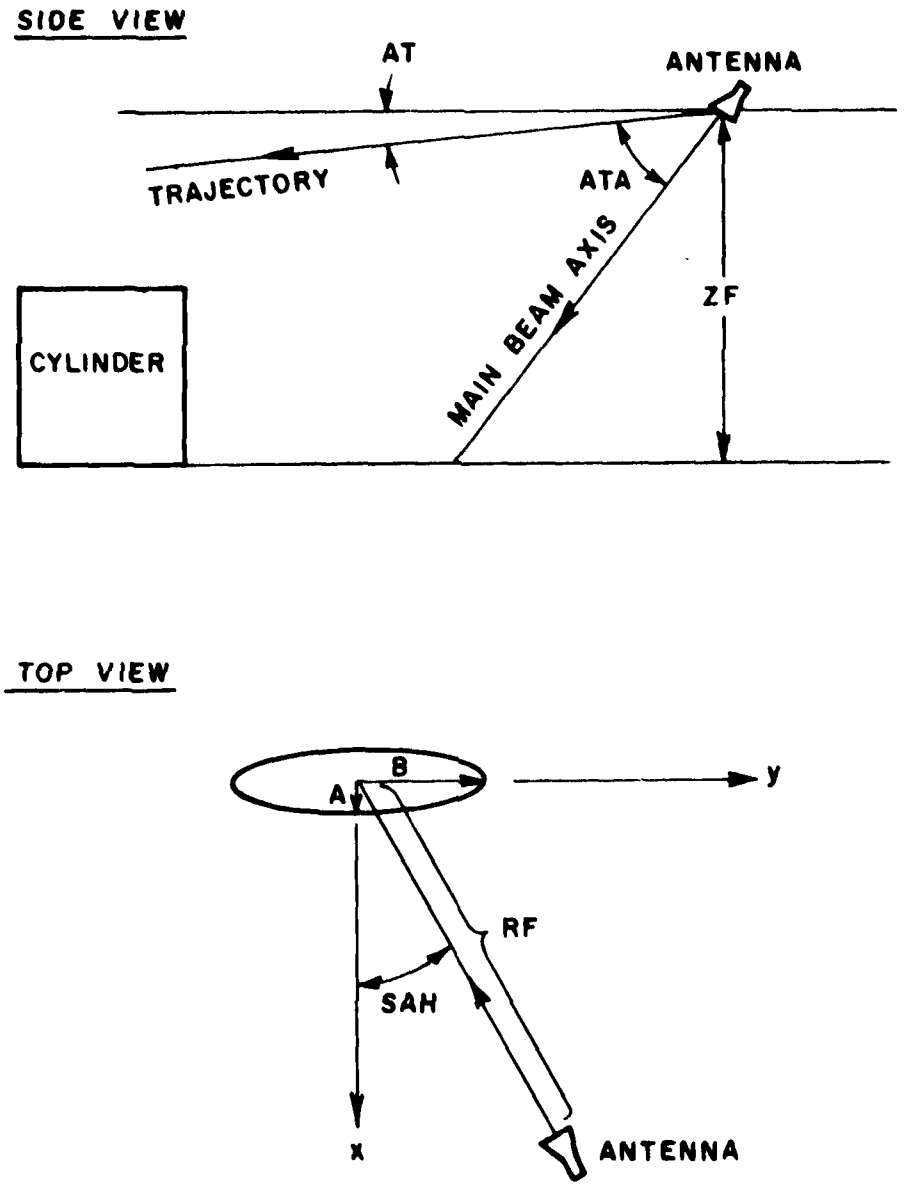

Figure 5-14. Configuration of elliptical cylinder at sea. patch size = 3 x 3. number of patches on each side of the illuminated area = 17. Vertical polarization is employed.

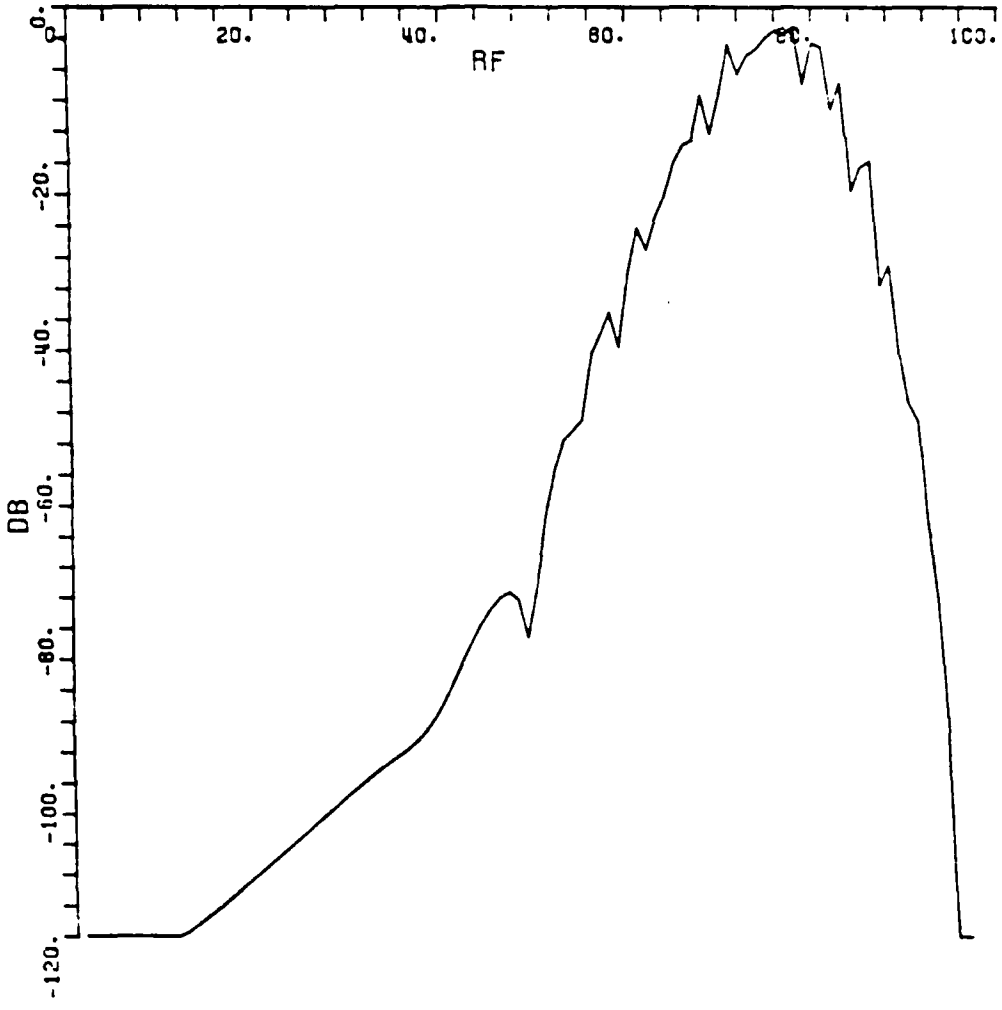

Figure 5-15. Voltage signature for the model of Figure 5-14. Horizontal trajectory (AT=0) at altitude 40.5 units (ZF=40.5). Ship dimension A=5, B=25 units. Antenna depression angle ATA= 60°. Aspect angle SAH=0°.

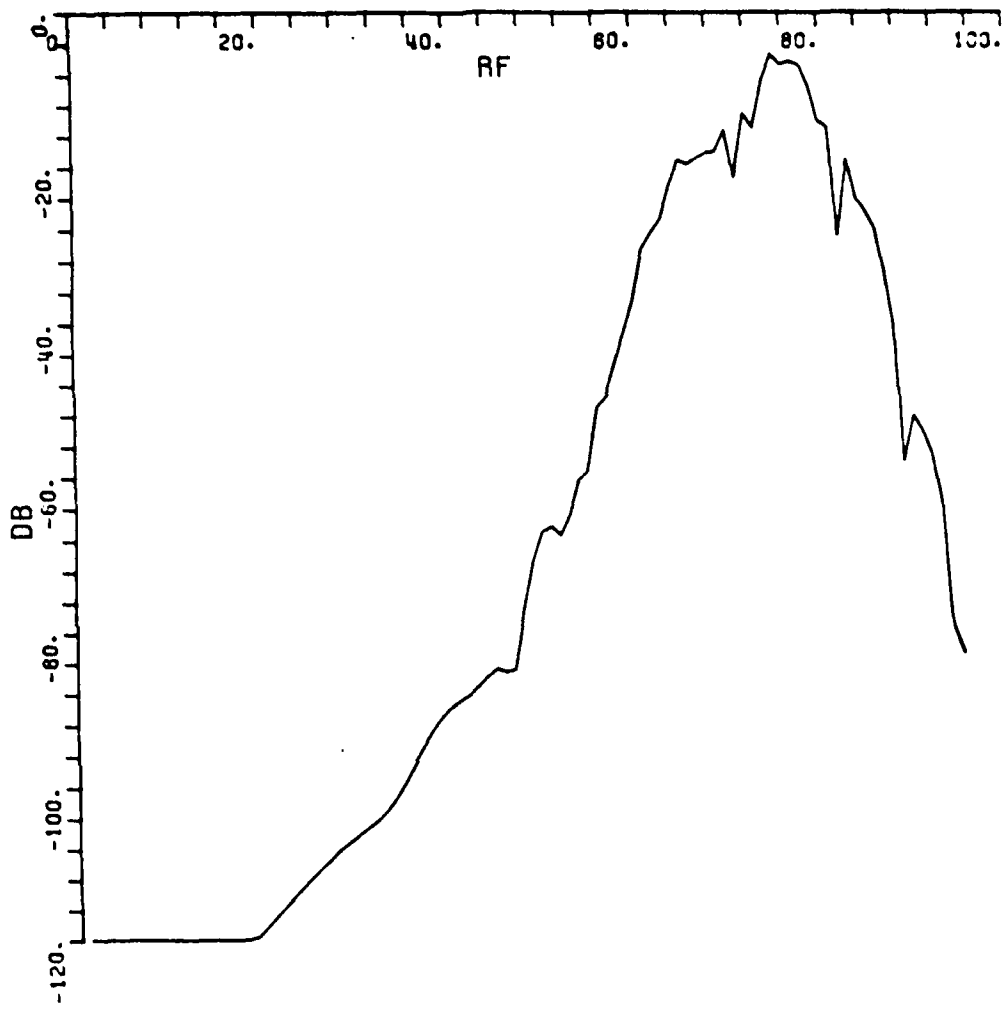

Figure 5-16. Voltage signature for the model of Figure 5-14. Horizontal trajectory (AT=0) at altitude 40.5 units (ZF=40.5). Ship dimension A=5, B=25 units. Antenna depression angle ATA= 60°. Aspect angle SAH=22.5°.

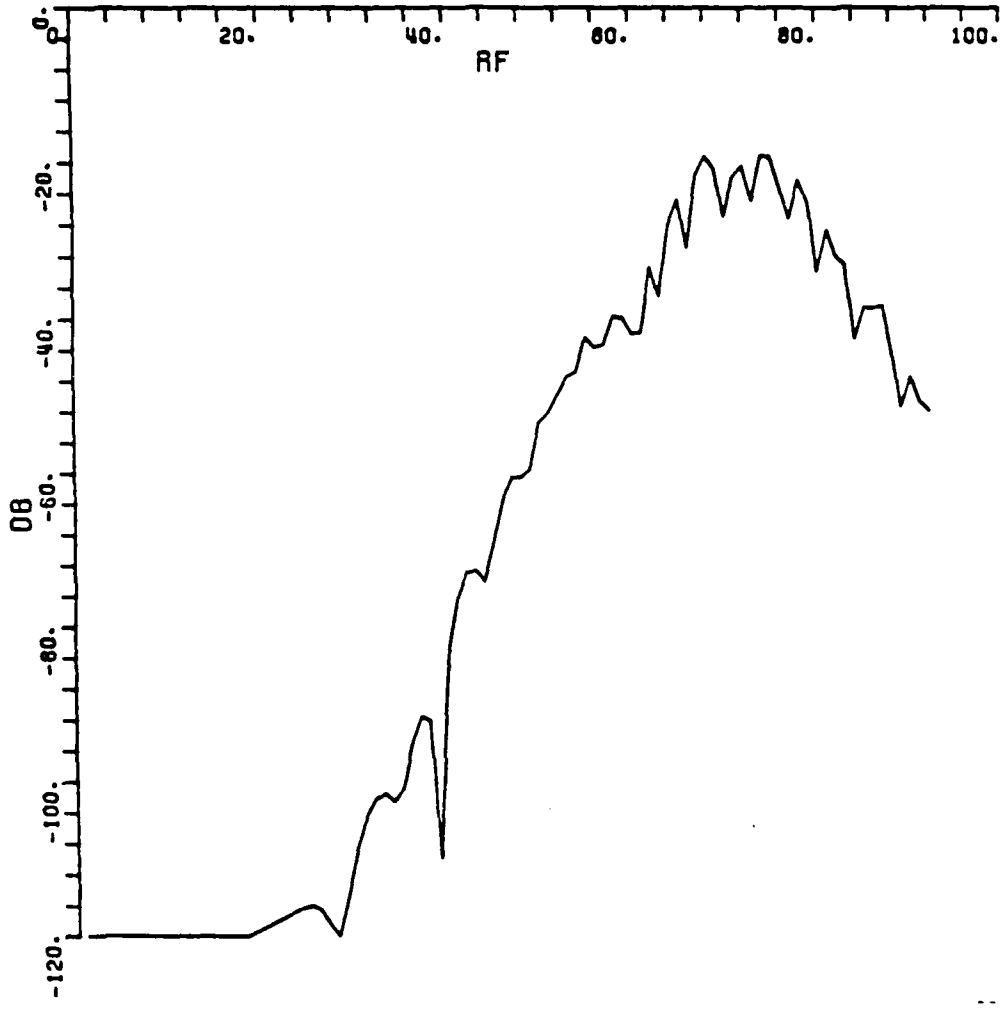

Figure 5-17. Voltage signature for the model of Figure 5-14. Horizontal trajectory (AT=0) at altitude 40.5 units (ZF=40.5). Ship dimension A=5, B=25 units. Antenna depression angle ATA= 60°. Aspect angle SAH=45°.

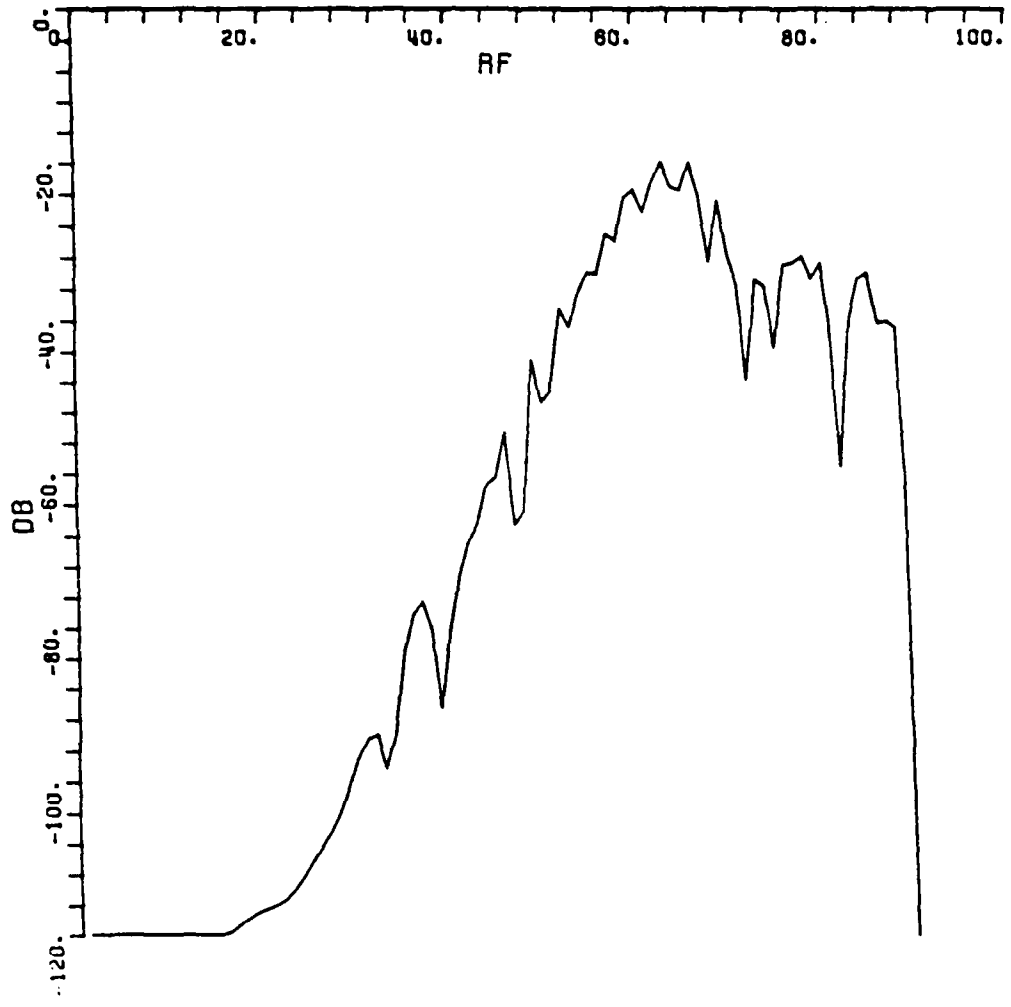

Figure 5-18. Voltage signature for the model of Figure 5-14. Horizontal trajectory (AT=0) at altitude 40.5 units (ZF=40.5). Ship dimension A=5, B=25 units. Antenna depression angle ATA= 60°. Aspect angle SAH=67.5°.

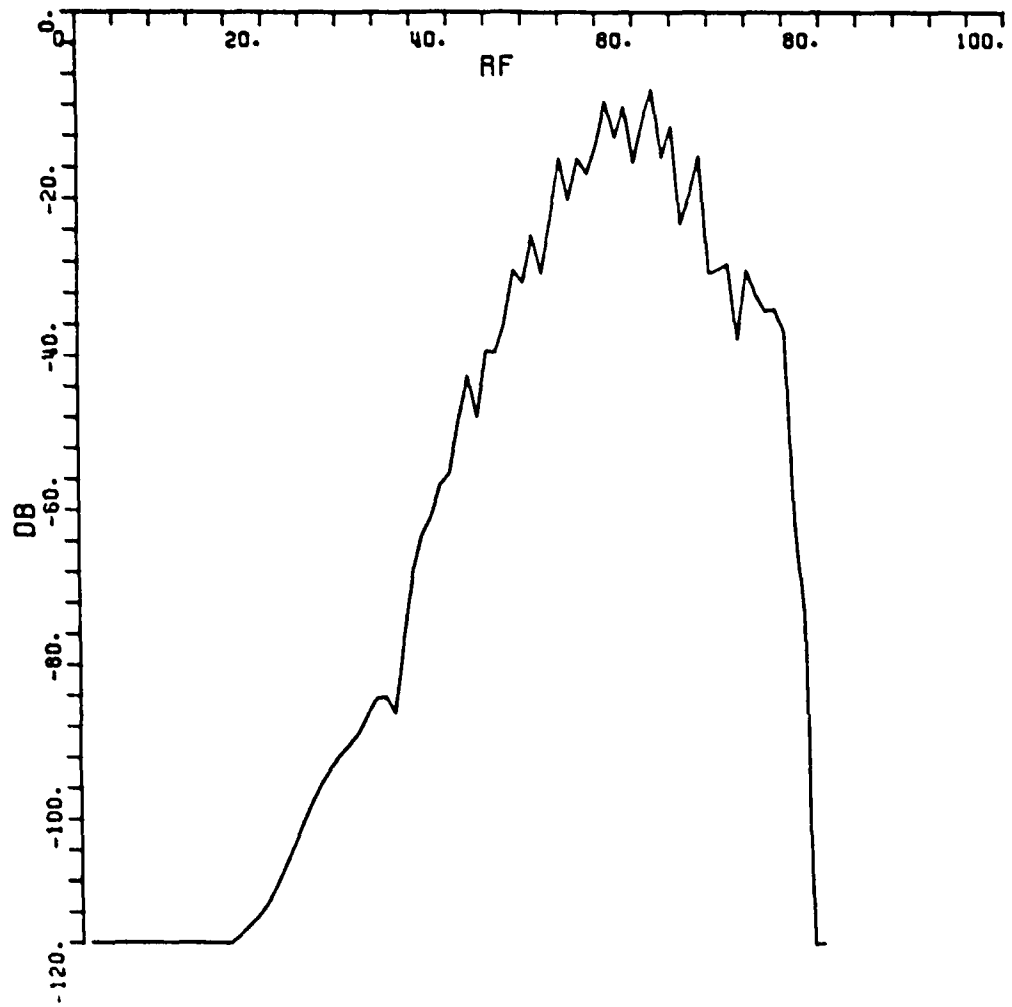

Figure 5-19. Voltage signature for the model of Figure 5-14. Horizontal trajectory (AT=0) at altitude 40.5 units (ZF=40.5). Ship dimension A=5, B=25 units. Antenna depression angle ATA= 60°. Aspect angle SAH=90°.

VI. SUMMARY AND CONCLUSIONS

In this report, two models for calculating the interaction between a radar system and a ship at sea, both adapted to short range encounters, have been presented. The first, developed to parallel a series of experiments at the Encounter Simulation Laboratory of the Naval Weapons Center, utilized a one-dimensional composite surface to model the sea, and a flat plate to model the ship. Four major scattering mechanisms were identified, and signatures calculated using first a physical optics formulation, and second a computationally more efficient formulation based on the geometrical theory of diffraction.

Signatures based on the physical optics method were in excellent agreement with measured signatures, and in both calculated and measured results the four components of the total signature could be clearly identified. The GTD signatures did not include the Bragg scatter component, but when compared with the physical optics signatures with Bragg scatter omitted, again excellent agreement was obtained. Thus it was concluded that the GTD method could produce accurate results for all but the Bragg back-scatter mechanism.

The second ship-sea model utilized a flat patch model for the ocean surface, with the scattering from each patch determined by the bistatic radar cross-section of the ocean. The ship was modelled by an elliptic cylinder. The major scattering mechanisms for this model (predominantly the double bounce corner mechanism) have been identified, and efficient methods for calculating the scattered fields (based on tracking stationary phase points on the ship structure) have been developed. Some preliminary signature calculations, showing the effect of the aspect angle of the ship target, have been made.

However, to produce realistic signatures for this model, two additional features must be programmed. The first is to include edge diffraction from the edges of the cylinder, and reflection from the top surface of the cylinder, as the trajectory passes over the target. The second is to include the back-scattering from each flat patch, in order to establish the clutter level, and typical clutter signatures, in the part of the trajectory preceding the encounter. Once these components are included, it should be possible to obtain realistic signatures for a variety of encounter geometries, for systems with any prescribed antenna patterns and polarizations, and receiver processing technique.

For future development of the model one must consider the use of a more realistic ship model, for example a hull formed from a section of an elliptic cone, perhaps with a roll angle, and surmounted by a rectangular or elliptic superstructure. In addition, one should consider a more realistic sea surface (including, e.g., a systematic bow wave structure as well as the random sea surface). The techniques developed in this report should permit the calculation of signatures which include both refinements in the ship model and the sea surface model suggested above.

REFERENCES

[1] W. H. Peake, "Electromagnetic Scattering from Composite Surfaces," Final Report 4229-2, January 1977, The Ohio State University ElectroScience Laboratory, Department of Electrical Engineering; prepared under Contract N60530-75-C-0216 for Naval Weapons Center.

[2] H. H. Porter, "A Modified Moment Method Calculation of the Electromagnetic Field Scattered by a Cylindrical Periodic Surface," Report 4428-1, December 1976, The Ohio State University ElectroScience Laboratory, Department of Electrical Engineering; prepared under Contract N60530-76-C-0186 for Naval Weapons Center.

[3] W. H. Peake and H. H. Porter, "Physical Optics Back Scatter from a Cylindrical Surface Illuminated by a Nearby Conical Beam Antenna," Report 4229-1, November 1976, The Ohio State University Electro-Science Laboratory, Department of Electrical Engineering; prepared under Contract N60530-75-C-0216 for Naval Weapons Center.

[4] D. E. Barrick, "Remote Sensing of Sea State by Radar," in Remote Sensing of the Troposphere, U. S. Department of Commerce, NOAA, August 1972.

[5] Daniel J. Ryan, "A Physical Optics Approach to the Electromagnetic Field Scattered by Simplified Ship-Sea Models," Report (78)4428-2, November 1977, The Ohio State University ElectroScience Laboratory, Department of Electrical Engineering; prepared under Contract No. N60530-76-C-0186 for Naval Weapons Center.

[6] R. G. Kouyoumjian and P. H. Pathak, "A Uniform Geometrical Theory of Diffraction for an Edge in a Perfectly Conducting Surface," Proc. IEEE, vol. 62, No. 11. November 1974.

[7] P. H. Pathak and R. G. Kouyoumjian, "The Dyadic Diffraction Coefficient for a Perfectly Conducting Wedge," Report 2183-4, 5 June 1970, The Ohio State University ElectroScience Laboratory, Department of Electrical Engineering; prepared under Contract No. AF 19(628)-5929 for Air Force Cambridge Research Laboratory. (AFCRL-69-0412) (AD 707827)

[8] C. H. Walter, Traveling Wave Antennas, Dover Publications, Inc., New York, 1965, pp. 46-84.

[9] R. J. Marhefka, "Analysis of Aircraft Wing-Mounted Antenna Patterns," Report 2902-25, June 1976, The Ohio State University ElectroScience Laboratory, Department of Electrical Engineering; prepared under Grant No. NGL 36-008-138 for National Aeronautics and Space Administration. pp. 91-100.